의학박사 학위논문

Modulation of long-term potentiation by firing patterns of granule cells in the hippocampal dentate gyrus

해마 치상회절 과립세포의 발화패턴에 의한 시냅스 장기강화 조절 기전

2023년 2월

서울대학교 대학원

의과학과 생리학 전공

김 윤 섭

A thesis of the Degree of Doctor of Philosophy

해마 치상회절 과립세포의 발화패턴에 의한 시냅스 장기강화 조절 기전

Modulation of long-term potentiation by firing patterns of granule cells in the hippocampal dentate gyrus

February 2023

The Department of Biomedical Sciences

Seoul National University

College of Medicine

Yoonsub Kim

해마 치상회절 과립세포의 발화패턴에 의한 시냅스 장기강화 조절 기전

지도 교수 호 원 경

이 논문을 의학박사 학위논문으로 제출함
2022년 10월

서울대학교 대학원
의과학과 생리학 전공
김 윤 섭

김윤섭의 의학박사 학위논문을 인준함
2023년 1월

위 원 장 _____ (인)

부위원장 _____ (인)

위 원 _____ (인)

위 원 _____ (인)

위 원 _____ (인)

Modulation of long-term potentiation by firing patterns of granule cells in the hippocampal dentate gyrus

by

Yoonsub Kim

A thesis submitted to the Department of Biomedical Sciences in partial fulfillment of the requirements for the Degree of Doctor of Philosophy in Medical Science at Seoul National University College of Medicine

January 2023

Approved by Thesis Committee:

Chair _____(Seal)

Vice Chair _____(Seal)

Examiner _____(Seal)

Examiner _____(Seal)

Examiner _____(Seal)

Abstract

Modulation of long-term potentiation by firing patterns of granule cells in the hippocampal dentate gyrus

Yoonsub Kim
The Department of Biomedical Sciences
The Graduate School
Seoul National University

High frequency burst firing is critical in summation of back-propagating action potentials (APs) in dendrites, which may greatly depolarize dendritic membrane potential. The physiological significance of burst firings of hippocampal dentate GCs in synaptic plasticity remains unknown. I found that GCs with low input resistance could be categorized into regular-spiking (RS) and burst-spiking (BS) cells based on their initial firing frequency (F_{init}) upon somatic rheobase current injection, and investigated how two types of GCs differ in long-term potentiation (LTP) induced by high-frequency lateral perforant pathway (LPP) inputs.

Induction of Hebbian LTP at LPP synapses required at least three postsynaptic APs at F_{init} higher than 100 Hz, which was met in BS but not in RS cells. The synaptically evoked burst firing was critically dependent on persistent Na^+ current, which was larger in BS than RS cells. The Ca^{2+} source for Hebbian LTP at LPP synapses was primarily provided by L-type calcium channels. In contrast, Hebbian LTP at medial PP synapses was mediated by T-type calcium channels, and could be induced regardless of cell types or F_{init} of postsynaptic APs. These results suggest that intrinsic firing properties affect synaptically driven firing patterns, and that bursting behavior differentially affects Hebbian LTP mechanisms depending on the synaptic input pathway.

Keywords : burst spiking, regular-spiking, Hebbian LTP, L-type voltage-gated Ca^{2+} channels, T-type voltage-gated Ca^{2+} channels, persistent Na^+ current, perforant pathway

Student Number : 2016-21976

CONTENTS

LIST OF FIGURES

INTRODUCTION

1. General Introduction

The hippocampus, the component of the limbic systems, is critically implicated in the high-order process of the brain, such as memory formation and cognitive function. It comprises dentate gyrus (DG), CA3 and CA1, the so-called hippocampal proper, forming a trisynaptic circuit. The DG is the first gate at which glutamatergic synaptic inputs from the entorhinal cortex (EC) are relayed. The primary afferent fibers from lateral and medial entorhinal cortex (LEC and MEC) layer II give rise to lateral and medial perforant pathways (LPP and MPP). LPP and MPP carry relatively more non-spatial and spatial information to DG, and innervate distal and intermediate parts of granule cell dendrites in the DG, respectively. Synaptic plasticity-based competitive learning together with the integration of spatial and non-spatial inputs in dentate granule cells (GCs, principal neurons of DG) was recently proposed to underlie the progressive refinement of spatial representation in DG (Kim et al., 2020). Axonal outputs of GCs after processing EC inputs were delivered to CA3 pyramidal neuron or hilar mossy cell through the mossy fiber (the axon of GCs), enabling them to convey information downstream or project

backward to GCs (associational/commissural, A/C inputs). In addition to excitatory inputs, GCs were innervated by GABAergic interneurons that control the activity of GCs. They were subdivided into several types by means of their location of somata, axonal projection or dendritic arborization (Hsu et al., 2016). Although GCs receive various excitatory or inhibitory signals, how they integrate multi-source inputs remains unclear.

2. Heterogeneous population of DG-GCs

The DG has a great number of neurons (~ 1 million in rodents) than their presynaptic sender EC layer II and postsynaptic receiver CA3 (1~2 hundred of thousand) as well as other hippocampal principal neurons. The outstanding number of GCs enable them to diverge (expansion recoding) and converge information flow from EC to CA3 regions. It allows hippocampal memory by orthogonalizing representation of cortical activity such as pattern separation, the ability to discriminate similar contexts.

Adult neurogenesis, one of the most striking features of DG, occurs throughout life. In the subgranular zone (SGZ), neural stem cells are differentiated and proliferated to immature GCs, and then undergo further maturation to become mature GCs. Although the rate of neurogenesis

declines with ages, adult-born cells are functionally integrated into hippocampal circuitry. Immature GCs are distinguished by electrophysiological characteristics from mature GCs, such as large input resistance (R_{in}), simple dendritic morphology and low LTP threshold (Lopez-Rojas and Kreutz, 2016) contributing to heterogeneity in GC population (immature GC: 5~10%, mature GC: 90~95%). Even though they receive GABAergic input mainly at the early stage, glutamatergic synapses from EC appear as maturation. Therefore, how they functionally contribute to hippocampal learning and memory is studied. On the other hand, mature GCs (mGCs) have hyperpolarized resting membrane potential (RMP, around −80 mV) and small R_{in} (<200 MΩ), resulting in poorly excitable. Furthermore, mGCs are known that strong stimulations are necessary to induce synaptic potentiation (Schmidt-Hieber et al., 2004), suggesting that they are less plastic. However, it is widely accepted that mGCs are involved in the high-order networks such as grid-to-place code conversion and storage of engrams rather than immature ones (Ryan et al., 2015; Zhang et al., 2020), which may require activity-dependent synaptic changes such as long term potentiation.

As well as maturity lineage, granule cells have more complex dendritic morphology and discrete intrinsic properties along with a transverse

(infrapyramidal–crest–suprapyramidal blade of GCL) axis (Claiborne et al., 1990). Therefore, elucidating neuronal complexity in DG is essential for understanding its functional network, considering that heterogeneity in cellular excitability could be one of the key mechanisms underlying the recruitment of principal cells to a neuronal ensemble or an engram for the representation and formation of memories (Pignatelli et al., 2019).

Sparse firing is a hallmark feature of the mGCs that they are much less excitable than any other neurons in the hippocampus (Alme et al., 2010). Recent *in vivo* recordings of GCs in DG revealed that a majority of GC spikes occurred in bursts, and that active GCs, which comprised only a minor subset of GCs, were morphologically mature and distinct from silent GCs. While these studies imply heterogeneity among dentate GCs, it remains to be understood how the difference in the excitability among heterogeneous groups of mature GCs is related to the difference in synaptic plasticity. Previously, it was noted that the initial frequency (F_{init}) of the first two action potentials (APs) upon somatic current injection is higher than the rest APs in mature GCs, and T–type voltage–dependent Ca^{2+} channels (T–VDCCs) contribute to the burst firing (Dumenieu et al., 2018). Burst firing enhances not only the reliability of pre–synaptic glutamate release (Lisman, 1997), but also postsynaptic Ca^{2+} signaling

required for synaptic plasticity (Kampa et al., 2006; Letzkus et al., 2006). Consistently, burst firing of principal cells plays diverse roles in different cortical regions such as place field formation in CA1 (Bittner et al., 2017), initiation of sharp waves in CA3 (Hunt et al., 2018), and switching thalamic network states for relaying subcortical inputs (Llinás and Steriade, 2006).

3. Dorsoventral axis

Despite of many disputes, it was generally thought that this long and curved structure has disparate functions along with the dorsoventral axis, where the dorsal (septal) hippocampus takes charge of spatial navigation while the ventral (temporal) manages emotional activity such as anxiety behaviors or stress related to the amygdala or hypothalamus (Fanselow and Dong, 2010; Strange et al., 2014). Also, molecular evidence with compartmentalized gene expression domains supported that stance (Dong et al., 2009). Recently, however, anatomical data or electrophysiological recordings demonstrated that there was a gradient in the hippocampus rather than binary aspects (Strange et al., 2014). At cellular levels, several studies show differences along the axis in CA1 pyramidal cells (PCs), which involves synaptic plasticity, electrophysiological characteristics such as RMP and R_{in}, and gene expression encoding

channels such as HCN, Kv4.2 (Marcelin et al., 2012) and Kv7/M (Hönigsperger et al., 2015). Moreover, morphological analysis determined that dendritic surface area and length are longer in dorsal than ventral CA1-PCs. In terms of circuit, they have different connectivity with extra- and intrahippocampal region, amygdala and CA3, respectively (Petrovich et al., 2001).

However, there were few studies about the characteristics of the DG along the axis. It was recently shown that field EPSP in medial perforant pathway (MPP) inputs is more readily potentiated in ventral dentate gyrus than dorsal segments (Schreurs et al., 2017), but further studies are required to understand the mechanisms underlying functional difference along the dorsoventral axis in dentate gyrus GCs.

4. Synaptic plasticity

GCs receive major cortical input through MPP or LPP at medial or distal dendrites. Each axon terminal has different short-term dynamics. When two stimuli are applied within a short interval under voltage-clamp mode in post-synaptic cells, the ratio of 2nd response to 1st response (paired-pulse ratio, PPR) would be facilitated or depressed. The PPR is known to measure release probability (P_r) at pre-synaptic terminals so that it is

also used as an index to monitor whether changes in synaptic strength are pre- or post-synaptic dependent mechanisms. A line of evidence showed paired-pulse depression (PPD) at MPP-GC synapses, but paired-pulse facilitation (PPF) at LPP-GC synapses (Colino and Malenka, 1993). It might result from the synaptotagmin 7, one of the calcium sensors which mediates asynchronous transmitter release and facilitation (Chen et al., 2017) is expressed more in the LPP than MPP (Jackman et al., 2016).

Since (Bliss and Lømo, 1973) demonstrated long-term potentiation (LTP) in the hippocampus by high-frequency stimulation (HFS), numerous experiments have been performed to understand LTP at PP-GCs synapses. Even these studies were performed primarily at MPP-GCs because it seems that the back-propagating action potential (AP) is highly attenuated at distal dendrite (Krueppel et al., 2011), so it could not trigger effective discharges to evoke Hebbian plasticity (Kim et al., 2018). Instead, dendritic sodium spikes, one of the local regenerative events, were turned out to be necessary for NMDAR-dependent LTP at LPP-GCs recently. However, little is known of cell type (among mature GCs) specific LTP at LPP-GCs.

5. Aim of this study

Bursting properties of GCs were previously reported *in vivo*, however, the functional significances were not understood in *ex vivo*. In acute slice, I found that there are two types of mature GCs: burst-spiking (BS) and regular-spiking (RS) GCs. I hypothesized that intrinsic firing pattern affects synaptically evoked AP firing. When I applied synaptic stimulation at high intensity (HFS_H). I found that a bout of HFS could induce LTP at LPP-GC synapse only when 3 APs were elicited at high frequency and LTP was induced prominently in BS-GCs. Even axonal T-type Ca^{2+} channels (Cav3.2) mediates bursting and LTP induction at MPP-GCs previously, I investigated other inward current determining intrinsic firing pattern, temporal summation and Ca^{2+} sources of LTP. As a result, I found Ca^{2+} influx through L-type Ca^{2+} channel specifically critical to induce LTP together with mGluR5 activation.

My next question was AP frequency is still effective signals in more proximal dendrite (MPP-GCs). Compared to LPP-GCs, T-type Ca^{2+} channel contribute to LTP induction at this synapse regardless of cell-types.

Beyond intrinsic firing pattern, I found uneven proportion of BS- and RS-GCs in dorsal DG. Given that differential hippocampal function along the

dorsoventral axis, I investigated their distribution in ventral DG. I found that BS-GCs were dominant in the dorsal DG, and their proportion was opposite in the ventral DG, suggesting their differential role together with cell-type specific LTP expression.

MATERIALS AND METHODS

1. Slice preparation and electrophysiology

Acute hippocampal slices (thickness, 350 μm) were prepared from the brains of 17- to 25-day-old Sprague-Dawley rats of either sex. Rats were anesthetized (isoflurane, Forane; Abbott) and decapitated immediately. All the experiments were approved by the University Committee Animal Resource in Seoul National University (Approval #: SNU-210825-6). All brains were obtained coronally for dorsal hippocampus or horizontally for ventral hippocampus (coronal sections located between 4.2 mm and 5.6 mm from the posterior end and transverse sections located 2.8 mm and 4.2 mm from ventral end of the right hemisphere). Slices were prepared in an oxygenated ice-cold sucrose-containing physiological saline using a vibratome (VT1200, Leica), incubated at ~36 ° C for 30 min, and subsequently maintained in the same solution at room temperature until the recordings. Recordings were performed at near- physiological temperature (33-35 ° C) in an oxygenated artificial cerebral spinal fluid (ACSF).

Patch pipettes were obtained from borosilicate glass capillaries (outer diameter = 1.5 mm, inner diameter = 1.05 mm) with a horizontal pipette

puller (P-97, Sutter Instruments). The open-tip resistance of patch pipettes was 2.5-4.5 MΩ for somatic recordings. Current- or voltage clamp recordings were performed with an EPC-10 USB Double amplifier (HEKA Elektronik). In current-clamp recordings, series resistance was 8-20 MΩ. Pulse protocols were generated, and signals were low-pass filtered at 3 or 10 kHz (Bessel), digitized (sampling rate: 20 kHz) and stored using Patchmaster software running on a PC under Window 10. Resting membrane potential (RMP) was measured immediately after patch break-in. Input Resistance (R_{in}) was determined by applying Ohm's law to the steady-state voltage difference resulting from a hyperpolarizing current step (-20 pA, 500 ms). Threshold for action potential was determined at points at which the derivative of voltage exceeded 40 V/s of somatic stimulations. Pipette capacitance and series resistance (R_s) compensation (bridge balance) were done at the beginning of current-clamp recordings. Recordings were stopped and discarded if R_S changed by more than 20% of R_{in} during the data acquisition.

All experiments were performed on visually identified mature GCs on the basis of the relatively large and round-shaped somata under DIC optics. GCs located at the superficial side of the GC layer in the suprapyramidal blade were purposely targeted. These cells had the average RMP of -81.6

± 0.7 mV and R_{in} of 115.7 ± 5.5 MΩ, that are similar to characteristic intrinsic properties of mature GC population (Schmidt-Hieber et al., 2004). Cells were filled with a fluorescent dye, Alexa Fluor 488 (50 μM, Invitrogen) at least 5 min and imaged with LED system (Thorlabs) mounted on an upright microscope equipped with a 60x water immersion objective lens (N.A. 1.0). In order for focal electrical stimulation (100 μs pulses of 5-40 V intensities) of the medial or lateral perforant pathways, a ACSF-filled glass pipette microelectrode (3-4 MΩ) was placed in the vicinity of intermediate or distal part of a visually identified dendrite (typically at <50 μm distance) of a GC under whole-cell patch. For evaluation of baseline synaptic responses, excitatory postsynaptic potentials (EPSPs) were evoked by applying a pulse every 10 s through a stimulation electrode. All experiments were performed in the presence of the GABA receptor antagonist picrotoxin (PTX, 100 μM) and CGP52432 (1 μM).

2. Calcium imaging

To measure Ca^{2+} influx at dendrites, cells were filled with two dyes, low-affinity Ca^{2+} indicator Fluo-5F (250 μM) to detect Ca^{2+} transient and Alexa Fluor 555 (50 μM) to visually guide subcellular structures. Pipette

resistance was 3~4 MΩ and series resistance was 10~20 MΩ. After obtaining whole cell configuration, I waited at least for 30 min before recordings were started to make both dyes diffuse fully into the distal dendrites. All processes were carried out using Metamorph imaging software and Igor Pro 6.37. Rectangular region of interest (ROI) and background region was determined. While imaging at 33 Hz under the nipkow spinning confocal microscope (real-time confocal system, CSU X1), I triggered Ca^{2+} transients (CaTs)by a pairing protocol (paring synaptic and somatic stimulations; See below). CaTs were shown as fractional changes of fluorescence, $\Delta F/F$, calculated as $((F_{ROI}-F_{background})-F_{prestim})/F_{prestim}$.

3. Stimulation protocols for the induction of long-term potentiation (LTP)

LTP was induced by either single bout of high-frequency stimulation (Remy and Spruston, 2007) of afferent fibers or a paring protocol. HFS consists of 10 stimuli at 100 Hz under current clamp mode. Depending on the stimulation intensity, HFS evoked subthreshold EPSP summation alone or additively post-synaptic APs, which are denoted as HFS_L and HFS_H, respectively. The pairing protocol is comprised of HFS followed by post-

synaptic injection of three suprathreshold current pulses (2 ms, 3 nA) at 100 Hz with a time delay (50 ms, LPP; 10 ms, MPP), similar to a protocol in (Watanabe et al., 2002). The time delay, 50 or 10 ms, was set based on the averaged synaptically evoked firing onset time. For LTP experiments, I monitored baseline EPSPs every 10 s at least for 5 min before applying LTP induction, after which I resumed the EPSP monitoring at least for 30 min. For off-line analysis, EPSP amplitudes were normalized to the mean of baseline values. A time course of normalized EPSP amplitudes was subject to binomial smoothing using a built-in function of IgorPro7 (WaveMetrics). The magnitude of LTP was evaluated as a mean of smoothed EPSP amplitudes measured 1 to 5 min or 26 to 30 min after LTP induction (denoted as LTP5 and LTP30, respectively).

4. Solutions and chemicals

The extracellular solution for dissection and storage of brain slices was sucrose-based solution (87 mM NaCl, 25 mM NaHCO3, 2.5 mM KCl, 1.25 mM NaH2PO4,7 mM MgCl2, 0.5 mM CaCl2, 10 mM glucose, and 75 mM sucrose). Physiological saline for experiments was standard ACSF (125 mM NaCl, 25 mM, NaHCO3, 2.5 mM KCl, 1.25 mM NaH2PO4, 1 mM MgCl2, 2 mM CaCl2, and 25 mM glucose).

For whole-cell recording, I used K^+ rich intracellular solution that contained 115 mM K-gluconate, 20 mM KCl, 10 mM HEPES, 0.1 mM EGTA, 4 mM MgATP, 10 mM Na2-phosphocreatine, and 0.3 mM NaGTP, pH adjusted to 7.2-3 with KOH (~300 mOsm). If necessary, 50 μM Alexa 488 were added to the internal solution to detect the dendrites. In subset of experiments for measuring persistent sodium current ($I_{Na.P}$), aCSF containing 20 mM tetraethylammonium chloride (TEA) and 0.2 mM $CdCl_2$ was used, and an internal solution in which K-gluconate and KCl were replaced with Cs-methanesulfonate and CsCl, respectively, at the same concentration.

5. Immunohistochemistry and morphological analysis

c-fos staining. Brains were perfused and post-fixed with 4% paraformaldehyde (Fujifilm) at 4 ° C overnight, and cryo-protected in 30% sucrose in 0.1 M PBS. After embedded in optimum cutting temperature compound (OCT), horizontal sections (50 μm thick) or coronal sections (50 μm thick) were obtained using a frozen sliding microtome (HM525 NX, Thermo Scientific) and stored in PBS at 4 ° C until processing for histology. Every $6^{th,}$ 12^{th},18^{th}, 24^{th} slices were selected for staining. Each was blocked with solution including 5% normal goat serum (NGS), 0.5%

TritonX−100 in PBS for 1 hr at room temperature. In primary or secondary staining procedures, 3% NGS and 0.5% TritonX−100 was used. Rabbit monoclonal anti−c−fos (1:1000; 2250S) was used as primary antibody. Cy5 conjugated goat anti−rabbit IgG (1:200, ab97077) was used as secondary antibody. Incubation of the primary antibodies was carried out at 4 ° C overnight, followed by incubation of secondary antibodies for 3 h at room temperature. Washing using PBS for 5 min × 3 times was performed between every step. After that, DAPI staining (1:10000) was operated for 10 min at room temperature. Slices were mounted with mounting media (M01), and coverslips were applied immediately.

Biocytin filling for morphology. GCs were filled with 0.2% biocytin (wt/vol) at least 20 min during whole−cell recording. The acute slices (thickness, 350 μm) were fixed overnight at 4° C in 4% paraformaldehyde (Fujifilm). After fixation, slices were washed for 10 min x 3 times with PBS and then permeabilized with 0.3% Triton X−100 in PBS. Subsequently, slices were treated with 0.3% Triton X−100 and 0.5% BSA in PBS to prevent non−specific staining. Next, they were treated with 0.3% Triton X−100 and streptavidin−Cy3 (1:500) in PBS and were again incubated overnight in 4° C. After washing steps, slices were finally mounted with DAKO S3023 medium, and coverslips were applied immediately.

Imaging. Confocal images were scanned through a 10x (N.A. 0.3), a 20x (N.A. 0.5) and a 40x (N.A. 0.5) water-immersed objective from FV1200 confocal microscope (Olympus Microscopy). For c-fos positive cell counting, all images have been processed using the open source Fiji software (ImageJ, NIH). To compensate the number of c-fos positive cells due to anatomical difference, the number of c-fos positive cell was divided by the number of DAPI positive cells (the number of granule cells). Because all granule cells were stained with DAPI, I estimate the number of cells instead of counting. I postulated the number of granule cells as the value determined by whole dentate gyrus pixels dividing by c-fos positive pixels. Branch orders were manually counted from a series of z-section images (z step: approx. 1 μm, 512 $\times$ 512 pixels) displayed using Fluoview software (FV31S).

RESULTS

1. Characteristics and distribution of two types of mature GCs.

Burst firing of dentate GCs has been observed both in vivo (Pernía-Andrade and Jonas, 2014) and ex vivo (Dumenieu et al., 2018), but its physiological significance in synaptic plasticity is not well understood. I examined firing patterns of mature GCs that have input resistance (R_{in}) less than 200 MΩ in response to somatic current injection. When I applied a step current just above action potential (AP) threshold (rheobase current) for 1 s in whole-cell current clamp mode, a group of cells generated APs in bursts, doublet in majority (82.8%, 18 of 22) and sometimes triplet (18.2%, 4 of 22), while others showed regularly spiking patterns (Fig. 1A). The histogram of initial firing frequency (F_{init}) showed bimodal distribution (Fig. 1B), so that I nominated cells with F_{init} under 50 Hz as regular-spiking (RS, gray), while cells with F_{init} over 50 Hz as burst-spiking (BS, red) neurons. The mean value for F_{init} was 10.6 ± 2.2 Hz (n = 18) in RS-GCs and 147.1 ± 11.2 Hz (n = 22) in BS-GCs. As the injection current increased, F_{init} increased in RS-GCs, and the

difference of F_{init} between RS− and BS−GCs gradually disappeared (Fig. 1Ca). Despite the remarkable difference in F_{init}, the number of APs during 1 s depolarization was not significantly different between two groups (Fig. 1Cb). Analyses of AP shapes revealed that the threshold voltage for AP generation was lower, AP duration was longer, and afterhyperpolarization (AHP) was smaller in BS−GCs compared to those in RS−GCs (Fig. 1D). No significant difference was found in passive electrical properties such as input resistance (R_{in}) and resting membrane potential (RMP) (Fig. 1E). Recent in vivo recordings of dentate GCs revealed that most active GCs fire in bursts and have higher maximal branch order (MBO) than silent GCs (Diamantaki et al., 2016; Zhang et al., 2020). To explore whether the bursting behavior is related to morphological properties of GCs, I counted the MBO from z−sections of confocal images of biocytin−filled RS− and BS−GCs (Fig. 2A). The MBO of majority of mature GCs was five, while cells with MBO higher than five was only found in BS−GCs and that with lower than 4 is only found in RS−GCs (Fig. 2B). The average MBO of BS−GCs was larger than that of RS−GCs, though the difference did not reach statistical significance (RS, 4.5 ± 0.3, n = 8; BS, 5.1 ± 0.1, n = 18, p = 0.1, Mann−Whitney test). Interestingly, in DG−GCs that have R_{in} more than 200 MΩ, which are less mature according to the criteria of maturation

(Schmidt-Hieber et al., 2004; Kim et al., 2018), bursting was very rarely observed (Fig. 2C), suggesting that burst firing is a characteristic feature of fully mature DG-GCs.

2. Subthreshold EPSP summation evoked by a single bout of HFS induces NMDAR-dependent LTP at LPP-GC synapses

To investigate whether intrinsic firing patterns have any effects on long-term synaptic plasticity, I recorded excitatory postsynaptic potentials (EPSPs) from RS-GCs or BS-GCs by stimulating lateral perforant pathways (LPP) in the presence of PTX (100 μM, a $GABA_AR$ blocker) and CGP52432 (1 μM, a $GABA_BR$ blocker) (Fig. 3A). After measuring the baseline EPSPs evoked by stimulation of LPP in a 10 s interval for about 5 min, a single bout of high frequency stimulation (HFS, 10 stimuli at 100 Hz) was applied. For the HFS, I tested two different levels of electrical stimulation intensity: low intensity to induce subthreshold response (HFS_L) and high intensity to evoke at least 3 APs (HFS_H). The average stimulation intensities of HFS_L and HFS_H were 15.6 ± 0.9 V (n = 21) and 25.7 ± 1.4 V (n = 18), respectively (Fig. 4A). The average amplitudes of baseline EPSPs induced by HFS_L and HFS_H were 5.9 ± 0.3

and 13.8 ± 1.0 mV, respectively (Fig. 4B). Temporal summations of EPSPs evoked by HFS_L reached their peaks between −60 mV and −40 mV at the 6^{th} or 7^{th} stimulus. RS− and BS−GCs showed no detectable difference in the temporal summation kinetics (RS, black; BS, red; Fig. 3B). Unexpectedly, the baseline EPSP amplitude of both groups was potentiated after HFS_L, and this potentiation lasted at least 30 min, indicating that HFS_L induces long−term potentiation (LTP) (Fig. 3C). I denoted this form of LTP as LTP_{Sub}, which stands for LTP induced by subthreshold stimulation. The increase in baseline EPSP amplitudes after HFS_L was not different between BS−GCs (36.9 ± 8.9%, n = 13) and RS−GCs (35.2 ± 5.3%, n = 12, p = 0.65). The magnitude of LTP_{sub} was correlated with the peak of EPSP summation ($r = 0.54$, $p < 0.001$), and significant LTP_{Sub} was induced when the peak was higher than −60 mV (Fig. 4C). To examine the involvement of NMDAR in LTP_{Sub}, I tested the effect of APV (50 μM, a NMDAR blocker) on EPSP responses and LTP expression induced by HFS_L. APV profoundly suppressed the baseline EPSPs as well as EPSP summation (Fig. 3E), and abolished LTP_{sub} (Fig. 3F). These results suggest that NMDAR−dependent LTP can be induced at LPP−GC synapses by a single bout of HFS that evokes only a subthreshold voltage response.

3. Postsynaptic burst firing is essential for Hebbian LTP at LPP–GC synapses

I then examined whether AP firings in response to HFS_H show any difference between BS and RS (Fig. 5A). The F_{init} of HFS_H–evoked APs was mostly higher than 100 Hz in BS–GCs (128.3 ± 6.9 Hz, n = 21, Fig. 5A). Furthermore, BS–GCs showed a moderate correlation between the F_{init} of synaptically evoked APs and that of APs evoked by somatic stimulation (r = 0.55, Fig. 5B). In contrast, the F_{init} of HFS_H–evoked APs in RS–GCs was significantly lower than that in BS–GCs (92.0 ± 9.9 Hz, n = 18; $p<0.01$; Fig. 5A). These results suggest that mechanisms underlying intrinsic firing pattern contribute to synaptically evoked firing pattern. When the 2nd HFS with higher stimulation intensity (denoted as 'HFS_H–2') was applied 10 min after HFS_L by which LTP_{Sub} has been already expressed both in RS and BS, HFS_H–2 induced further potentiation of EPSPs in BS–GCs, but not in RS–GCs (Fig. 5C). The time course of this LTP induced by HFS_H–2 is shown as the EPSP amplitudes normalized to the EPSP amplitude just before applying HFS_H–2 (Fig. 5D). The increase in the EPSP amplitude at 30 min was 44.0 ± 4.8% (n = 7) in BS–GCs, but negligible in RS–GCs (–4.2 ± 7.0%, n = 12; $p < 0.001$). These results indicate that BS–GCs express Hebbian LTP (denoted as

LTP_{AP}) distinct from NMDAR-dependent LTP_{Sub}. There was a positive correlation between LTP_{AP} magnitudes and F_{init} of synaptically evoked APs (Fig. 5E). To investigate whether EPSP potentiation is induced by increased local dendritic excitability or by increased postsynaptic AMPA receptors, I examined changes of EPSC after HFS_H-2. I found that EPSC amplitudes also potentiated in BS-GCs (75.2 ± 18.7%, n = 3) and its magnitude was comparable with LTP magnitude in EPSP, confirming that HFS_H-2 eliciting more than 3 APs induces synaptic potentiation (Fig. 5F). However, when only 1 or 2 APs were elicited by HFS with medium intensity (HFS_M), LTP was not induced or not maintained even in BS-GCs (-10.6 ± 12.8%, n = 6; Fig. 5G-H), indicating that postsynaptic AP bursts comprised of at least 3 APs at the frequency higher than 100 Hz are essential for the induction of LTP_{AP}.

To further test the importance of AP frequency for induction of LTP_{AP}, I applied a pairing protocol, in which 10 EPSPs were evoked by HFS_L coinciding with 3 APs at 100 Hz evoked by brief current injection to the soma (Fig. 6A, see Methods). The pairing protocol successfully induced LTP regardless of cell types with no significant difference in the LTP magnitude between RS-GCs and BS-GCs (Fig. 6B). These findings show that RS-GCs could express LTP_{AP} as if BS-GCs did as long as high

frequency APs are paired with synaptic stimulation. Therefore, I did not distinguish BS and RS but pooled the BS and RS data when I analyzed LTP response induced by pairing protocol (gray trace in Fig. 6C). LTP was not induced when intracellular Ca^{2+} was chelated with a high concentration of BAPTA (10 mM, Fig. 5I). Next, I examined the condition for LTP_{AP} induction. When 3 APs were associated at 50 Hz to mimic firing of RS–GC, LTP was not induced (Fig. 6D). As well as postsynaptic firing frequency, LTP was not induced when presynaptic firing frequency was lower to 50 Hz. Collectively, my results indicate that both post– and pre–synaptic burst firing ($\geq$ 100 Hz) is required to activate Hebbian LTP, and suggest that Ca^{2+}–dependent mechanisms underlie this form of LTP.

4. NMDAR mediates the early phase LTP and facilitates EPSP summation at LPP–GC synapses

To examine whether LTP_{AP} shares the same Ca^{2+} source with NMDAR–dependent LTP_{sub}, I tested the effect of APV. Because APV profoundly suppressed EPSP summation (Fig. 3E), in the presence of APV it was difficult to generate 3 APs even with high intensity stimulation, and thus LTP_{AP} was not induced (Fig. 6F), indicating that NMDAR current is critical for EPSP summation to elicit high frequency AP generation. However, I

could induce LTP by the pairing protocol in the presence of APV (Fig. 6G). Because the time course of LTP development was distinct from that of control pairing-induced LTP (brown vs. gray traces in Fig. 6G), I compared the LTP magnitudes in the APV conditions with the control values for the early and late phases. To this end, I measured normalized EPSP amplitudes averaged over 1 to 5 min and over 26 to 30 min after HFS, and denoted as LTP5 and LTP30, respectively. LTP5 in the APV conditions was significantly lower, while LTP30 was not different compared to the corresponding control values [LTP5, 8.6 ± 5.5% vs. 25.7 ± 4.6%, $p<0.05$; LTP30, 46.4 ± 12.7% vs. 52.62 ± 7.71%, $p = 0.57$; APV ($n = 11$) vs. Control ($n = 14$), Mann-Whitney test. Fig. 6H]. These results suggest that the contribution of NMDAR to Hebbian LTP as Ca^{2+} source is limited to the early phase LTP at LPP-GC synapses, whereas it is essential for EPSP summation and AP burst generation.

5. Dorsal DG is more active than ventral dentate gyrus

I examined whether the relative proportion of BS- and RS-GCs differs along the hippocampal dorso-ventral axis. I found that BS-GCs were dominant in the dorsal DG, and their proportion was opposite in the ventral DG. Among 232 recorded neurons in dorsal DG, 148 (64%) GCs were

identified as BS−GCs, while only 8 (18%) out of 45 GCs were BS−GCs in ventral DG, indicating that the dorsal DG harbors more BS−GCs compared to the ventral DG (Fig. 7A).

What is the functional significance of uneven cell distribution along the axis and different LTP expression levels (see Fig.5D) in GCs *in vivo*? Because dorsal and ventral DG are separately involved in spatial memory and emotion, c−fos^{+} ensembles of neurons in each region are newly activated in a task−specific way (Wang 2020 NC). In addition, deficiency of c−fos causes impaired long−term memory and synaptic plasticity in CA1 (Alexander 2003 JN). Since it is not well known about the cell−type specific expression of c−fos in DG, I performed immunohistochemistry of c−fos as a neural activity marker at two divided regions (dorsal and ventral) in DG (Fig.7A). Before fixation, animals were exposed to novel objects for 1 hr. The number of c−fos^{+} cells was divided by the DAPI^{+} cells of DG to compensate for the difference in cell density due to anatomical locations. The ratio of c−fos^{+} cells in dorsal DG is higher than that in ventral DG (dorsal: 1.5 ± 0.2%, n = 8; ventral: 0.9 ± 0.1%, n = 6; $p<0.05$; Fig. 7B). This data is consistent with the result reported previously (Scharfmann 2019). Taken together, dorsal DG, which has mainly BS−GCs, is more active than ventral DG. Additionally, we found

that c-fos^{+} cells were mostly observed in the outer GCL (where mGCs are located) of the suprapyramidal blade. Next, I hypothesized that c-fos^{+} cells would be BS-GCs because they were frequently observed in the outer GCL. To address this question, I obtained whole-cell recordings of GCs using the biocytin-contained intracellular solution in acute slices before the fixation process (Fig.7C). However, I found that almost all GCs show the positive signal of c-fos specifically in the dentate gyrus, not CA1 or CA3, making it difficult to identify co-localization of c-fos and biocytin labeling and thought to be unreliable results itself. Also, signals seemingly had a gradient from the border of the hilus to the outer GCL into decline. This phenomenon might be result from acute slice preparation procedure, but it remains to be clarified.

6. T-VDCC contributes to the late phase LTP by facilitating AP bursts at LPP-GC synapses

I showed that burst firing evoked by somatic rheobase current injection (called intrinsic burst firing) has correlation with the F_{init} of synaptically evoked APs which is crucial for LTP_{AP} induction (Fig. 5). I investigated whether ion channel mechanisms underlying intrinsic burst firing also contribute to LTP_{AP}. Since T-VDCC is known to mediate intrinsic bursting

in DG-GCs (Dumenieu et al., 2018), I investigated the role of T-VDCCs in burst firing behavior and LTP_{AP} induction in BS-GCs. Bath application of $NiCl_2$ (50 μM, the blocker of T-VDCC) significantly reduced F_{init} of intrinsic burst firing (Control, 171.8 ± 13.3 Hz; $NiCl_2$, 38.1 ± 8.89 Hz, n = 9; $p<0.01$; Wilcoxon signed-rank test; Fig.8A). When the bursts were synaptically evoked, $NiCl_2$ partially but significantly reduced the F_{init} (Control, 128.3 ± 6.9 Hz, n = 21; $NiCl_2$, 91.2 ± 3.5 Hz, n = 13, $p<0.001$, Mann-Whitney test; Fig. 8B). Nevertheless, in the presence of 50 μM Ni^{2+}, temporal summation of EPSPs evoked by HFS_L was little affected (n = 10, p = 0.11; Fig. 8C), and HFS_H was able to induce LTP_{AP} in the BS cells (Fig. 8D). In contrast to APV, the early phase LTP was preserved in the presence of Ni^{2+} [LTP5 of Ni^{2+} (n = 7) vs. control (n = 7), 24.9 ± 5.6 vs. 27.5 ± 6.3%, p = 0.90], but no further increase in the EPSP amplitudes was observed (Fig. 8D vs. Fig. 5D), and thus LTP30 was lower than the control (20.4 ± 7.7 vs. 44.6 ± 5.7%, $p<0.05$, Fig. 8D). Because Ni^{2+} lowered the F_{init} of synaptically evoked AP bursts, I tested if suppression of late LTP_{AP} can be rescued by pairing protocol. The mean value for LTP30 measured after the pairing protocol was slightly lower but not significant compared to pairing-induced LTP in control (32.6 ± 13.0 vs. 52.6 ± 7.7% , n = 8, p = 0.19; Fig. 8E), suggesting partial or little

contribution of T-VDCC to the LTP_{AP} induction. Similar to HFS_H-induced LTP, LTP5 was not different from the control value (25.0 ± 8.2 vs. 25.7 ± 4.6%, p = 0.97). These results suggest that T-VDCC primarily contributes to the late phase LTP_{AP} by enhancing F_{init}.

7. Persistent Na^+ current amplifies LPP-evoked EPSP summation and is essential for burst firing

Previously, it was shown that T-VDCC in axon initial segment plays a key role in intrinsic burst firing of GCs (Dumenieu et al., 2018). Whereas Ni^{2+} abolished intrinsic bursts (Fig. 8A), it partially reduced F_{init} of synaptically evoked bursts with little effect on EPSP summation (Fig. 8B-C), implying a possible involvement of dendritic channels in synaptically evoked AP bursts. As a candidate ion channel regulating intrinsic and synaptically evoked bursts, I examined persistent sodium current ($I_{Na.P}$). In CA1 pyramidal cells, $I_{Na.P}$ amplifies subthreshold EPSPs leading to spatially tuned firing (Hsu et al., 2018). I measured F_{init} of intrinsic bursts in BS-GCs after applying riluzole (10 μM), a typical $I_{Na.P}$ blocker (Chen et al., 2005; Yue et al., 2005; Hsu et al., 2018). Riluzole significantly reduced F_{init} of the intrinsic bursts (Fig. 9A) similar to its effect in CA1 pyramidal neurons (Chen et al., 2005). In addition, it markedly suppressed

summation of HFS_L–evoked EPSPs (Fig. 9B). Due to the substantial inhibition of EPSP summation by riluzole, it was not possible to synaptically evoke AP bursts, even with very high stimulation intensity, and LTP was not induced (Fig. 9C). When 10 EPSP bursts induced by HFS_L were paired with 3 APs (pairing protocol), however, the late phase LTP was completely rescued (LTP30, 43.3 ± 14.7 vs. 52.6 ± 7.7%, n = 10, p = 0.34 compared to pairing–induced LTP in control, Mann–Whitney test; Fig. 9E). The rescue of late phase LTP by the pairing protocol suggests that burst APs coincident with synaptic inputs is essential for the late LTP induction. By contrast, early phase LTP (LTP5) was significantly lower than the control value (LTP5, 9.6 ± 6.7 vs. 25.7 ± 4.6%, n = 10, $p<0.05$), resulting in the LTP time course similar to that in the APV condition (Fig. 5J–K). This similarity may be explained by assuming that Ca^{2+} influx through NMDAR mediate the early phase LTP, and that $I_{Na,P}$ contributes to NMDAR activation in distal dendrites by amplifying EPSP summation, which cannot be compensated by somatic bursts.

Since riluzole showed profound effects on both intrinsic and synaptically evoked firings, I hypothesized that intrinsic bursting behavior is mainly affected by somatic $I_{Na,P}$, while synaptically evoked AP firings are affected by dendritic $I_{Na,P}$. To test this, I examined the effect of focal puff

application of riluzole (Fig. 9F). Peri-somatic puff application of riluzole (50 μM) considerably reduced the F_{init} of intrinsic burst firings in BS-GCs, whereas dendritic puff had no effect at all (Fig. 9G). On the contrary, the EPSP summation was profoundly diminished by dendritic puff, but not by peri-somatic puff of riluzole (Fig. 9H). These results support my hypothesis for the preferential roles of somatic and dendritic $I_{Na,P}$ on the intrinsic and synaptically evoked firing behaviors, respectively. Since BS-GCs have higher F_{init} both for intrinsic and synaptically evoked APs than RS-GCs, I tested whether difference in $I_{Na,P}$ density underlies the different bursting behavior between these two GC types. To measure I_{NaP} in the identified GC type, I first examined the AP responses to somatic rheobase current injection using the standard intracellular solution, carefully withdrew the pipette, and then re-patched the same cell again with Cs^+- based pipette solution in the presence of Cd^{2+} (200 μM) and TEA (20 mM) in the bath solution to inhibit Ca^{2+} and K^+ currents (Fig. 9I). I quantified $I_{Na,P}$ in each type of neurons using a slowly rising ramp voltage command protocol from a holding potential of -70 mV to 0 mV for 6 seconds in voltage-clamp configuration. In consistent with my hypothesis, the peak amplitude of $I_{Na,P}$ in BS-GCs was significantly larger than that in RS-GCs (Fig. 9J).

8. L-type Ca^{2+} channel is a major Ca^{2+} source for LTP induction but little contributes to firing properties.

Above results indicate that NMDAR and T-VDCC partially contribute to LTP_{AP}, and that $I_{Na.P}$ is essential for intrinsic and synaptically evoked burst firings in BS-GCs. L-type VDCC (L-VDCC) is known as a calcium source for NMDAR-independent slowly developing LTP induced by 200 Hz tetanic stimuli at CA3-CA1 synapses (Grover and Teyler, 1990; Bayazitov et al., 2007). I studied the role of L-VDCC in burst firing and LTP_{AP} induction. Distinct from drugs tested above, nimodipine (10 μM), an L-VDCC blocker, had no effect on the F_{init} of APs evoked by somatic current injection (Fig. 10A). Moreover, nimodipine affected neither EPSP summation induced by HFS_L nor the F_{init} of APs evoked by HFS_H (Fig. 10B-C). Nevertheless, the late phase of LTP_{AP} was abolished in the presence of nimodipine (LTP30, -3.1 ± 11.0 vs. $44.6 \pm 5.7\%$, $p<0.01$, $n = 6$, Fig. 10D). Furthermore LTP30 was not rescued by the pairing protocol (LTP30, -2.9 ± 10.3 vs. $52.6 \pm 7.7\%$, $p<0.01$, $n = 7$, Fig. 10E), indicating that calcium influx through L-VDCC during AP bursts is essential to induce LTP_{AP}. Although the LTP5 values for HFS_H- and pairing-induced LTP were marginally lowered (HFS_H, $7.2 \pm 9.3\%$, $n = 6$, $p = 0.10$; Pairing protocol, $4.3 \pm 8.2\%$, $n = 7$, $p = 0.08$, Mann-Whitney test), the early

increase in normalized EPSP was transient, suggesting that it belongs to short-term potentiation (STP) which decayed within 3 min (Lisman, 2017). Therefore, these results indicate that L-VDCC mediate both early and late phase LTP but not STP. Next, I evaluated Ca^{2+} transients (CaTs) evoked by the pairing protocol at distal dendrites. GCs were filled with low Ca^{2+} affinity dye, Fluo-5F (250 μM), and Alexa 555 (50 μM) to trace dendrites visually, and then imaged on the confocal microscope (Fig. 10F). Using focal stimulation methods (Materials and Methods), I could easily identify a dendritic branch at which the amplitudes of CaTs (dF/F of Fluo-5F) were distinctly higher than others probably indicative of receiving synaptic inputs. Comparing CaTs in control with those in nimodipine conditions, I found that amplitudes of CaTs were slightly but significantly decreased by nimodipine (Fig. 10G). Such a small contribution of L-VDCC to dendritic CaTs despite a distinct role in downstream Ca^{2+} signaling has been previously observed at CA3-CA1 synapses, too (Yasuda et al., 2003).

9. LTP_{AP} is not fully expressed without HFS_L.

So far, I have described that the NMDAR-dependent LTP_{sub} and the L-type dependent LTP_{AP} were exclusively induced by HFS_L-1 and HFS_H-2

in BS−GCs (Fig.5C). I focused on mechanisms that are involved in dividing two LTP induction. To answer this question, I applied HFSH−1, which evokes more than 3 APs to both GCs. Unexpectedly, EPSP amplitudes were potentiated after HFS_H−1, but did not reach to sum of LTP_{sub} and LTP_{AP} magnitudes in Fig. 5C in BS−GCs (HFS_H−1, 63.1 ± 9.6%, n = 8; HFS_L−1+HFS_H−2, 108.5 ± 8.2%, n = 5, $p<0.05$; Fig.11A). Whereas, those magnitudes were not significantly different in the case of RS−GCs (HFS_H−1, 39.6 ± 10.3%, n = 8; HFS_L−1+HFS_H−2, 26.5 ± 12.9%, n = 5). Furthermore, the LTP magnitude of BS−GCs was slightly reduced in the presence of nimodipine (Nimo, 54.0 ± 10.8%, n = 6, p = 0.66). These data suggested that weak contribution of L−VDCC when HFS_L−1 is directly applied. Therefore, it is indicated that L−VDCC is more activated after HFS_L−1. Indeed, in the presence of Bay K (10 uM, L−VDCC activator), EPSP amplitude was potentiated as much as magnitudes enhanced by a step−wise manner (Bay K, 130.7%, n = 1). Nevertheless, the mechanisms that makes L−VDCC more activated need to be investigated.

10. LTP induction at MPP−GC synapses is not affected by firing pattern

Above results indicate that LTP at LPP−GC synapses can be induced by two distinct mechanisms: NMDAR−dependent subthreshold LTP and compound Hebbian LTP, and that the latter heavily depends on activation of L−VDCC resulting from postsynaptic AP bursts. I investigated whether MPP−GC synapses share the same LTP mechanisms with those of LPP−GC synapses. I recorded MPP−evoked baseline EPSPs using an electrode placed in the middle of the molecular layer in a 10 s interval for about 5 min before HFS was applied (Fig. 12A). The stimulation intensity was adjusted so that the peaks of EPSP summation evoked by 100 Hz 10 stimuli remained subthreshold level (around −60 mV ~ −40 mV) (denoted as HFS_L). Average stimulation intensity of HFS_L was 10.9 ± 0.6 V, which is significantly smaller than that used for LTP_{sub} induction at LPP−GC synapses (15.6 ± 0.9 V, Fig. 4A). The EPSP summation usually reached its peak at 2^{nd} or 3^{rd} stimulation and declined afterwards, consistent with the characteristic short−term depression at MPP−GC synapses (Colino and Malenka, 1993). RS− and BS−GCs showed no detectable difference in their subthreshold EPSP responses to HFS_L (RS, black; BS, red; Fig. 12B). Unlike NMDAR−dependent LTP_{sub} at LPP−GC synapses, HFS_L did

not induce LTP either in RS− or BS−GCs [RS, 17.7 ± 8.8% (n = 5); BS, 9.5 ± 7.0% (n = 6); p = 0.66; Fig. 12C]. Moreover, the 1st EPSP amplitude was not affected by APV (MPP, n = 6, p = 0.075; LPP, n = 10, p = 0.047), and the APV effect on the area of EPSP summation was weaker compared to LPP−GC synapses (MPP, p = 0.03; LPP, p < 0.01; Fig. 12D−E). Lower contribution of NMDAR current may be attributable to lower local depolarization at synaptic sites and/or to lower density of NMDAR at the middle part of GC dendrites compared to that at distal dendrites.

When the stimulation intensity was increased to evoke 3 APs, F_{init} was higher in BS−GCs than RS−GCs (Fig. 12F), suggesting that intrinsic bursting mechanisms affect synaptic bursting induced by MPP stimulation, as was shown for LPP−evoked bursts. In spite, LTP_{AP} was induced similarly in both BS and RS [LTP30: BS, 43.8 ± 3.6% (n = 5); RS, 32.1 ± 10.2% (n = 7); p = 0.20; Fig. 12G]. Because of no difference between RS and BS in the LTP magnitudes and time courses, the LTP data from the two cell types were merged for following comparison with LTP under different conditions. At MPP−GC synapses, the LTP magnitude was not correlated with F_{init} (Fig. 12H, r = 0.20, p = 0.47), suggesting that AP frequency is not critical for the LTP_{AP} induction at MPP−GC synapses. To further test this idea, we tried to induce LTP using a pairing protocol, in

which HFS_L was paired with 100 Hz or 50 Hz three APs evoked by somatic stimuli to mimic firing of BS− or RS−GCs, respectively. We found that the LTP magnitudes were not significantly different between them (LTP30: 100 Hz (n = 7) *vs.* 50 Hz (n = 7), 56.1 ± 14.6 *vs.* 31.2 ± 6.3%, p = 0.26, Fig. 12I). I tested whether EPSP potentiation is induced by increased local dendritic excitability or postsynaptic AMPA receptors. I found that EPSC amplitudes also potentiated in both GCs (45.9 ± 9.7%, n = 5) and its magnitude was comparable with EPSP data.

11. Hebbian LTP at MPP−GC synapses is mediated by T−VDCC

I characterized the Ca^{2+} source mediating Hebbian LTP (LTP_{AP}) at MPP−GC synapses. Consistent with the small contribution of NMDAR to EPSP summation at MPP synapses (Fig. 12D), AP bursts were readily evoked by HFS_H of MPP in the presence of APV (Fig. 13A). In the presence of APV, the late phase LTP magnitude was not different from the control value [LTP30, 42.7 ± 11.7 vs. 37.0 ± 6.2%, APV (n = 6) vs. control (n = 12), p = 0.75], but the early phase LTP was significantly inhibited [LTP5, 8.6 ± 3.1 (n = 7) vs 31.8 ± 5.8% (n = 14), p<0.01] (Fig. 13A), suggesting that NMDAR contributes to short−term potentiation and early phase LTP,

but not to the late phase LTP at MPP−GC synapses.

Nimodipine had no significant effect on MPP−evoked AP generation similar to LPP synapses. In stark contrast to LTP_{AP} at LPP−GC synapses (Fig. 10), LTP_{AP} at MPP−GC synapses was not affected by nimodipine (LTP5, 28.7 ± 4.0%, p = 0.95; LTP30, 48.5 ± 20.0%, n = 4, p = 0.77; Fig. 13B), but abolished by $NiCl_2$. $NiCl_2$ significantly reduced the F_{init} of MPP−evoked APs (Fig. 13C), and abolished the late phase LTP at MPP−GC synapses (LTP30, 6.0 ± 5.3%, n =5, p = 0.009, Fig. 13D). $NiCl_2$ marginally lowered LTP5 (12.8 ± 6.8%, n = 5, p = 0.07), but the early increase in normalized EPSP was not sustained (Fig. 13D), reminiscent of the nimodipine effects at LPP synapses (Fig. 10D). Moreover, the pairing protocol did not rescue the Ni^{2+} effect on LTP_{AP} at MPP−GC synapses [Pairing protocol−induced LTP; LTP5, 7.8 ± 5.1 vs. 30.3 ± 6.7%, p = 0.017; LTP30, 8.0 ± 6.0 vs. 35.4 ± 8.2%, Ni^{2+} (n = 7) vs. control (n = 7), Fig. 13E], indicating that LTP_{AP} at MPP−GC synapse is mediated by Ca^{2+} influx through T−VDCC.

12. HFS_H activates mGluR5 signaling pathways at LPP−GC synapses

Pairing presynaptic 10 stimuli at lower frequency (50 Hz) with 3

postsynaptic APs at LPP–GC synapses failed to bring significant potentiation (Fig. 6E). Moreover, LTP_{AP} was not induced by 1 Hz repeated pairing of a single presynaptic stimulation with postsynaptic AP bursts for 5 min (pre– and post–synaptic sequence, 5 ms interval; Fig. 14), indicating that LTP_{AP} at LPP–GC synapses critically depended not only on postsynaptic but also on presynaptic bursts. The requirement of presynaptic bursts is consistent with the condition for spillover of synaptically released glutamate thereby peri–synaptic mGluRs could be activated (Okubo and Iino, 2011). For studying downstream signaling of LTP_{AP}, I adopted the pairing protocol to avoid possibility that the test drugs may affect postsynaptic AP bursts. In the presence of MPEP (25 μM), the paring protocol did not induce LTP at LPP–GC synapses (Fig. 15A). Because mGluR5 is a G_q–coupled G protein receptor, I tested involvement of phospholipase C (PLC) in the downstream signaling for induction of LTP. After pre–incubation of the slice with U–73122 (an inhibitor of PLC, 2 μM) at least for 30 min, LTP_{AP} was abolished (Fig. 15B). However, in the blockade of the mGluR1, the other family of group 1 mGluR, LTP was not abolished (Fig. 15C), indicating mGluR1 activation is not necessary to induce LTP.

In stark contrast to LTP_{AP} at LPP–GC synapses, that at MPP–GCs was

not affected by MPEP, U73122 and LY367385 (Fig. 16A–C). This result is consistent with a previous report that more intense stimulation is required for induction of mGluR–dependent LTP at these synapses (Wu et al., 2008).

13. Endocannabinoid signaling is not associated with LTP_{sub} and LTP_{AP} at LPP–GCs

Recently, it was shown that two trains of HFS (1 s at 100 Hz, 1 min interval) of LPP induced presynaptic LTP through activation of mGluR5 and endocannabinoid–dependent retrograde signaling (Wang et al., 2016). I tested if LTP_{AP} observed in the present study shares the same mechanism with the LTP form reported in Wang et al (2016). I could induce LTP at LPP–GC synapses by the pairing protocol even in the presence of AM251, a CB_1 inverse agonist (Fig. 17A), arguing against involvement of endocannabinoid signaling in the induction of LTP_{AP} at LPP–GC synapses. Even though I applied two trains of HFS (1 s at 100 Hz) as Wang et al. (2016), LTP was still induced in the presence of AM251 (Fig. 16) at both stimulation intensities that evoked only subthreshold compound EPSP and that evoke postsynaptic APs (Fig.

17B-C). I confirmed that depolarization induced suppression of inhibition (DSI), which mediated by endocannabinoid signaling, is abolished by AM251 (Fig. 17D).

DISCUSSION

1. Ionic mechanisms underlying Hebbian LTP at LPP and MPP synapses

One of main findings of the present study is that induction of Hebbian LTP (LTP_{AP}) at LPP-GC synapses is critically dependent on high frequency burst firing of pre- and post-synaptic cells. Induction of Hebbian LTP required at least three post-synaptic APs firing at 100 Hz or higher frequency, and thus Hebbian LTP at LPP-GC synapses occurred preferentially at BS-GCs compared to RS-GCs. To scrutinize the mechanisms underlying LTP_{AP} at LPP-BS synapses, I differentiated whether different inward currents contribute to LTP_{AP} by enhancing postsynaptic AP bursts (burst-enhancer) and/or providing Ca^{2+} influx mediating LTP_{AP} (LTP-mediator). To this end, when an inward current blocker suppressed HFS_H-induced LTP_{AP}, I tried to induce LTP_{AP} by applying the pairing protocol in the presence of the blocker. When LTP_{AP} was rescued by the pairing protocol, I regarded it as 'burst-enhancer', and otherwise as 'LTP-mediator'. The other factor to be considered was the time course of LTP_{AP}. As shown in Fig. 5D and G, LTP_{AP} in BS-

GCs was comprised of three components: STP, early and late LTP. STP decayed within 3 min, and early and late phases of sustained potentiation lasted more than 30 min (early and late LTP, respectively) (Lisman, 2017). Because the mechanism underlying STP and early phase LTP are known to be different from that underlying the late phase LTP at CA3–CA1 synapses (Grover and Teyler, 1990; Bayazitov et al., 2007), I measured normalized EPSP amplitudes averaged over early (1 – 5min) and late (26 – 30 min) intervals of the LTP time course, and regarded the former (LTP5) and the latter (LTP30) as magnitudes of STP plus early LTP and late phase LTP, respectively. I examined contributions of NMDAR, T–VDCC, $I_{Na,p}$ and L–VDCC under this framework. For the late phase LTP_{AP} at LPP–GC synapses, only L–VDCC met the condition for the 'LTP–mediator', and other inward currents seem to contribute as a burst–enhancer. For the early phase LTP, the LTP magnitude induced by the pairing protocol was marginally or significantly lower in the presence of blockers of NMDAR and L–VDCC, implying that these two Ca^{2+}–influx channels may mediate the early phase LTP. The differential involvements of NMDAR and L–VDCC in early and late LTP has been shown in CA3–CA1 synapses (Grover and Teyler, 1990). Whereas NMDAR–dependent LTP was rapidly expressed in the postsynaptic locus,

NMDAR-independent LTP developed more slowly, depended on L-VDCC and expressed in presynaptic locus (Bayazitov et al., 2007). These ionic mechanisms of LTP at CA3-CA1 synapses are different from those at LPP-GC synapses, in that L-VDCC contributes to both early and late LTP, while NMDAR does to early LTP. The locus of LTP expression at LPP-GC synapses remains to be investigated. In contrast to LPP-GC synapses, Hebbian LTP at MPP-GC synapses was mediated by T-VDCCs, and BS-GCs had no privilege for induction of LTP at MPP synapses. The requirement of T-VDCC is consistent with (Dumenieu et al., 2018), which showed that deletion of $Ca_V3.2$ gene reduced LTP at MPP-GC synapses.

2. Ionic mechanisms underlying AP bursts

Most neuronal burst firings are associated with prominent afterdepolarization (ADP), which can be generated by dendritic Ca^{2+} spikes and/or axo-somatic slow activating inward current. The dendritic contributions to burst firing has been found in hippocampal and neocortical pyramidal neurons (Larkum et al., 1999; Chen et al., 2005; Raus Balind et al., 2019). The burst firing of GCs seems to be axo-somatic type, because axo-somatic T-VDCCs played a crucial role (Dumenieu et al., 2018). I found that not only T-VDCCs but also $I_{Na,P}$ contribute to the burst firings

in GCs (Fig. 8 and 9). $I_{Na,p}$ is a small fraction of Na^+ current that slowly inactivates and exhibits low threshold for activation compared to larger fast and transient fraction of Na^+ current. It has been suggested that $I_{Na,p}$ not only generates ADP (Yue et al., 2005) but also amplifies synaptic current (Schwindt and Crill, 1995). It is very likely that contribution of $I_{Na,p}$ to ADP underlies intrinsic burst firing, while $I_{Na,p}$ contributes to synaptically evoked AP by amplifying EPSP summation. Consistent with this view, I showed that the F_{init} of intrinsic bursts in BS-GCs was reduced by local puff of riluzole to the soma, but not by that to the dendrites, suggesting contribution of somatic $I_{Na,p}$. By contrast, dendritic $I_{Na,P}$, but not somatic $I_{Na,P}$, was responsible for enhancing EPSP summation and LPP-evoked AP bursts (Fig. 9G-H). On the other hand, block of T-VDCC using $NiCl_2$ resulted in only partial reduction of F_{init} of LPP-evoked AP bursts (Fig. 8C), whereas it had stronger effect on MPP-evoked burst firing (Fig. 13C), implying higher density expression of T-VDCC on proximal dendrites compared to distal dendrites. This view is supported by my findings that T-VDCC plays as an LTP-mediator in MPP synapses whereas it plays only a partial role in LTP_{AP} induction at LPP synapses (Fig. 8D-E and Fig. 13D-E).

3. The role of post-synaptic high frequency bursts in Hebbian LTP at LPP synapses

At LPP-GC synapses, LTP_{AP} was induced preferentially in BS cells and the F_{init} of synaptically evoked burst firing was highly correlated with the LTP_{AP} magnitude (Fig. 5E). Why high frequency bursts are required for LTP_{AP} induction at LPP-GC synapses? Considering that L-VDCC is a major Ca^{2+} source (Fig. 10), although L-VDCC has little influence on both synaptic and AP responses, it is likely that activation of L-VDCC requires high frequency back-propagating APs. A previous study in L5 neocortical pyramidal neurons may provide a hint for addressing the question. (Larkum et al., 1999), using dual patch recordings at apical dendrite and soma in a single neocortical L5 pyramidal neuron, discovered nonlinear summation of back-propagating APs (bAPs) at distal apical dendrites: As somatic APs back-propagated along apical dendrites, they were attenuated in amplitude and broadened in width. While low frequency bAPs underwent only such linear attenuation, as the bAP frequency increased above a critical point (100 Hz), bursts of four bAPs summated to readily reach the threshold for activation dendritic Ca^{2+} channels (Larkum et al., 1999). I imagine that a similar scenario may be involved in the L-VDCC dependent dendritic Ca^{2+} signaling evoked by a burst of three somatic APs

in GCs. The broadening and attenuation of bAPs at intermediate dendrites has been shown in my previous study (Kim et al., 2018). Summation of bAPs at distal dendrites remains to be elucidated in GCs, though it would be a challenging task considering the feasibility of patching on the distal dendrites of GCs.

4. Hebbian vs. non-Hebbian LTP at LPP-GC synapses

Previously I studied a different form of LTP at LPP-GC synapse, which was critically dependent on dendritic Na^+ spikes and activation of NMDA receptors (Kim et al., 2018). This form of LTP was induced by theta burst synaptic stimulation (TBS) of LPP, but not by the standard spike time-dependent plasticity (STDP) protocol, which is pairing EPSP with a single somatic AP (Kim et al., 2018). The LTP shown in (Kim et al., 2018) could be induced even without somatic APs as long as TBS elicited dendritic spikes. In contrast, a burst of 100 Hz three APs was required for the induction of LTP_{AP} not only in the pairing protocol but also in the induction protocol of synaptic stimulation alone (HFS_H). Therefore, the LTP forms shown in my previous and present studies belong to non-Hebbian and Hebbian LTP, respectively. The strong attenuation of back-propagating somatic APs along the dendrites of mature GCs might be responsible for

the no LTP induction by the standard STDP protocol (Kim et al., 2018). The results of the present study suggest that postsynaptic AP bursts may overcome the strong dendritic attenuation probably by summation of bAPs in distal dendrites to activate L-VDCCs.

Remarkably, only a single bout of HFS (10 stimuli at 100 Hz) was sufficient for induction of Hebbian LTP. I previously used TBS (4 repeats of 5 Hz 10 bouts of HFS) for induction of dendritic spike-dependent LTP in (Kim et al., 2018). The key differences in the LTP induction protocols between these two studies are not only the number of HFS bouts but also the LPP stimulation intensity. The baseline EPSP in my previous and present studies were 7.1 ± 0.5 mV and 13.8 ± 1.0 mV, respectively, indicating that the stimulation intensity required for LTP_{AP} is stronger than that for dendritic spike-dependent LTP.

The subthreshold LTP discovered in the present study has not been described before. It is unique in that ten stimuli which evoked only subthreshold EPSP summation can induce NMDAR-dependent LTP as long as the peak EPSP summation was higher than −60 mV. Because such weak stimuli have been routinely employed to characterize the baseline properties of synapses, the subthreshold LTP has been ignored in my previous study (Kim et al., 2018). Therefore, the dendritic spike-

dependent LTP described in (Kim et al., 2018) has been induced on the top of subthreshold LTP. Given that subthreshold LTP is mediated by NMDA receptors, the local EPSP summation elicited by high frequency LPP inputs may result in large local depolarization at distal dendrites sufficient for activation of NMDARs, even if it does not elicit somatic APs or dendritic spikes (Note that there was no evidence for dendritic spikes in somatic recordings during the subthreshold LTP induction). Recent in vivo whole-cell recordings in GCs revealed that majority of GCs were under the influence of spatially tuned PP synaptic inputs while only minority of them exhibited spatially tuned firings (Zhang et al., 2020). In light of these findings, subthreshold LTP at LPP-GC synapses might extensively occur over the GC population receiving brief bursts of LPP inputs independent of postsynaptic firings.

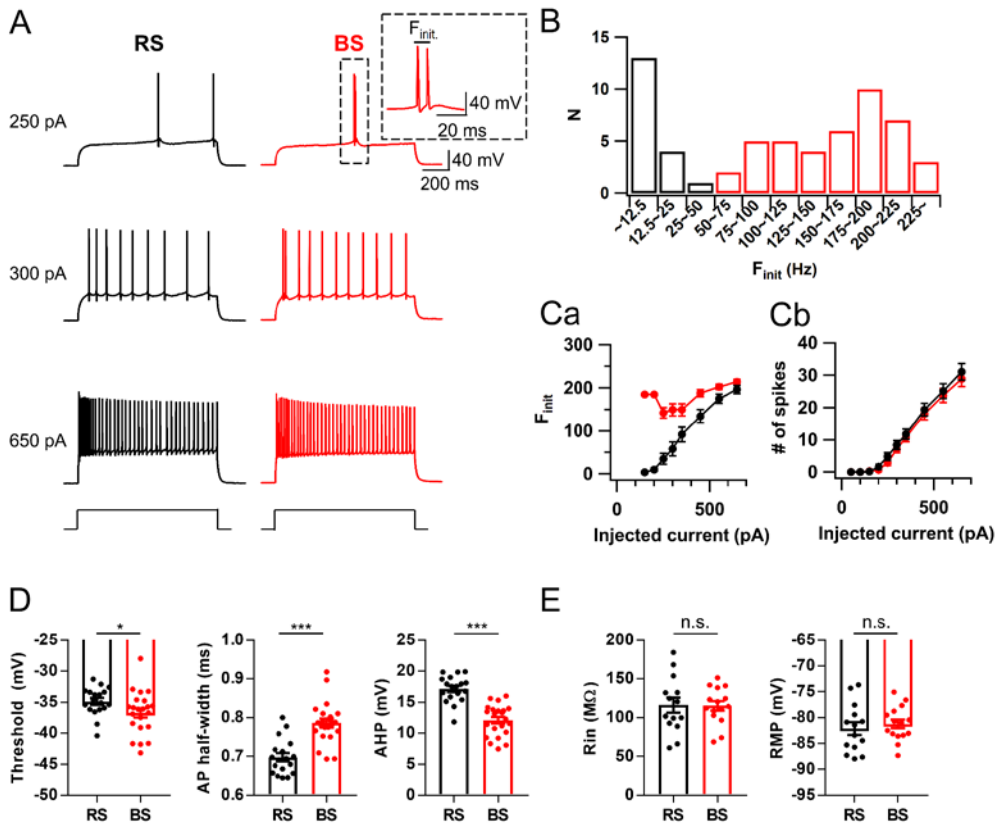

Fig. 1, Intrinsic properties of regular-spiking (RS) and burst-spiking (BS) mature granule cells. A: Representative voltage responses of RS (black) and BS (red) cells to somatic current injection of 250, 300 and 650 pA (1s duration). *Inset*, initial firing of BS-GCs at expanded time scale. Initial firing frequency (F_{init}) was measured as the frequency of first two APs at rheobase current injection. B: Bimodal distribution of F_{init} among mature GCs. Mature GCs were divided into RS and BS with the reference frequency of 50 Hz (RS/BS, n = 18/42). Ca-b: F_{init} (*a*) and spike numbers

(*b*) of RS and BS cells as a function of injected current amplitude (from 50 to 650 pA). F_{init} of RS cells increased steeply compared to those of BS-GCs. The general excitability of both GCs was not different throughout all steps (RS/BS, n = 18/22). **D**: Summary bar graphs for analyses of 1st AP waveform evoked by somatic rheobase current injection into RS and BS cells. Mean values for AP threshold were −34.9 ± 0.5 mV in RS and −36.7 ± 0.7 mV in BS (*p<0.05). For afterhyperpolarization (AHP) amplitudes, 17.1 ± 0.5 mV in RS and 12.0 ± 0.5 mV in BS (***p<0.001). For half-width duration, 0.70 ± 0.01 ms in RS and 0.79 ± 0.01 ms in BS (***p<0.001; RS/BS, n = 18/22). **E**: Input resistance (R_{in}; RS, 116.1 ± 9.6 MΩ; BS, 115.3 ± 6.1 MΩ) and resting membrane potential (RMP; RS, −82.1 ± 1.3 mV; BS, −81.2 ± 0.9 mV) were not different between RS and BS. Error bars indicate S.E.M. *p<0.05. ***P<0.001. n.s., not significant (p>0.05).

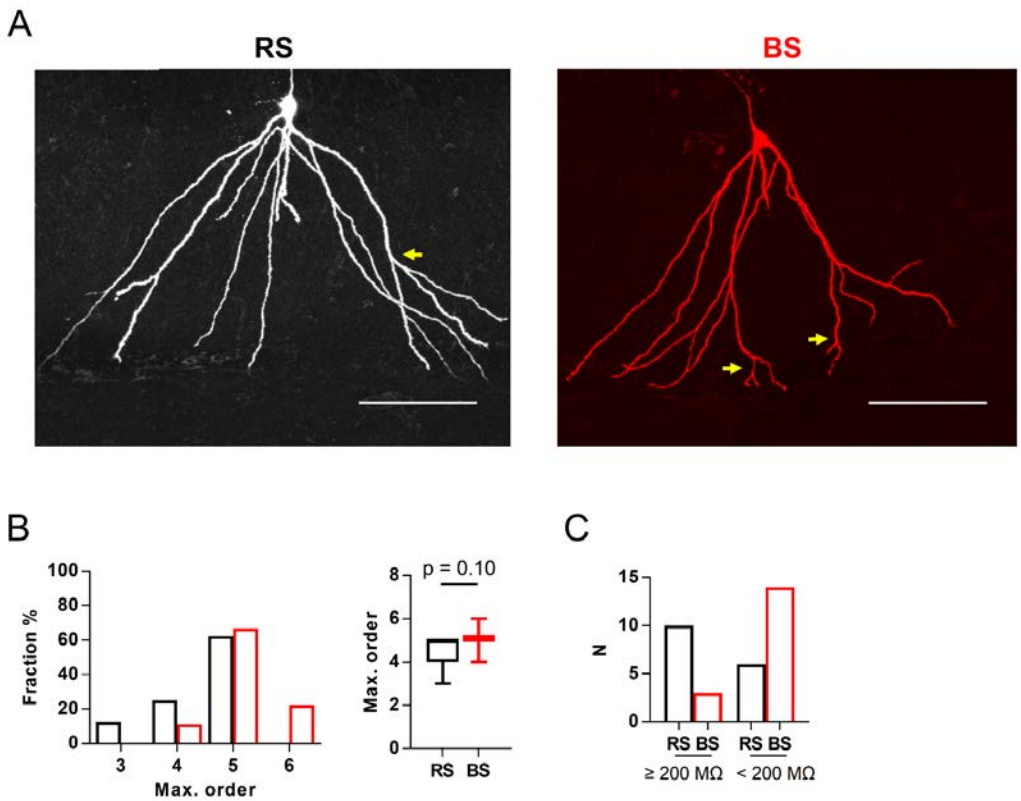

Fig. 2, Morphology analysis of RS− and BS−GCs. A: Representative biocytin−filled RS− (*left*) and BS−GC (*right*). Yellow arrows indicate the maximal dendritic branching points. Scale bar, 100 μm. **B:** Distributions (*left*) and mean values (*right*) for maximal dendritic branch order in RS (black) and BS (red) cells (RS, 4.5 ± 0.3, n = 8; BS, 5.1 ± 0.1, n = 18, p = 0.10). **C:** Proportion of RS and BS cells depends on the GC maturity. BS cells were more frequently found in the group of mature GCs (R_{in} < 200 MΩ) compared to the less mature GC group (R_{in} ≥ 200 MΩ; RS/BS, n = 16/17).

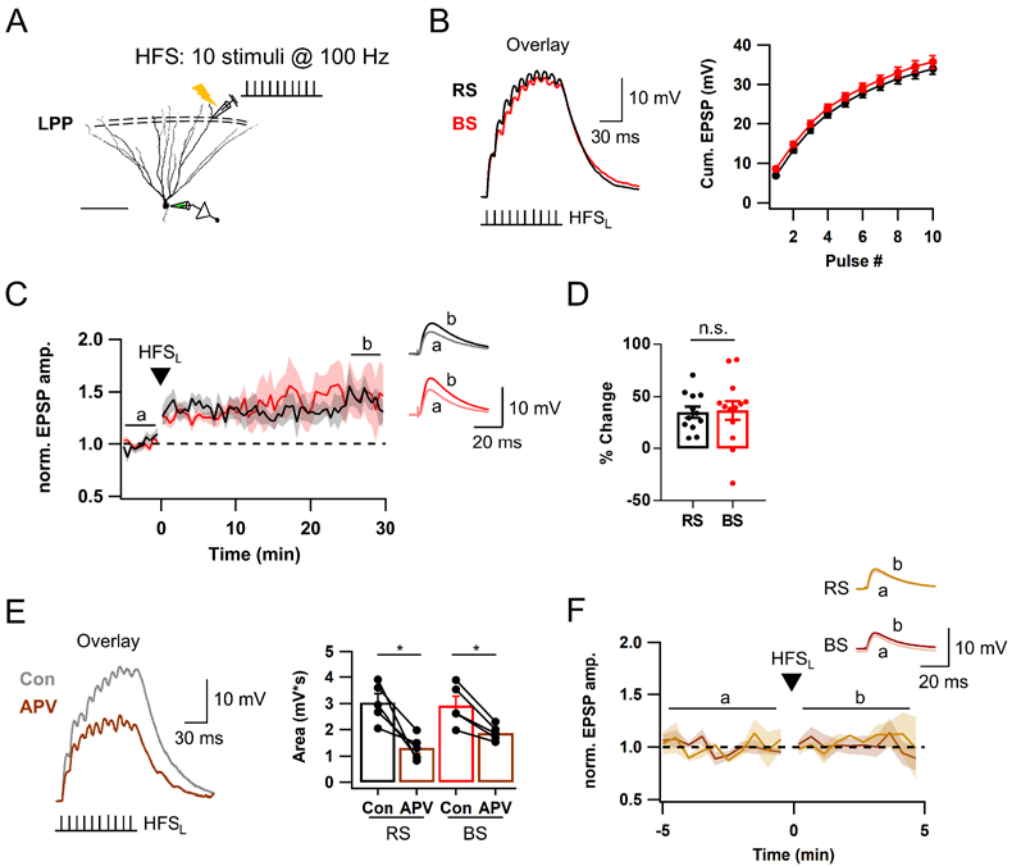

Fig. 3, NMDAR-dependent LTP at LPP-GC synapses is induced by a single bout of high frequency stimulation (HFS) at subthreshold level. A: Schematic diagram illustrating the recording configuration for synaptic stimulation and whole cell recording of mature GC. Lateral perforant pathway (LPP) in outer molecular layer (OML) was electrically stimulated by a bout of HFS (10 stimuli at 100 Hz). Scale bar is 100 μm. B: HFS_L-evoked subthreshold responses of RS- (black) and BS-GCs (red) (*left*), and their cumulative EPSP amplitudes (*right*). C: Time courses of

normalized EPSP amplitude before and after HFS_L (same as in *B*). Each point represents averaged value for adjacent 3 EPSP amplitudes (30 s binned). Black dashed line denotes baseline EPSP. *Inset*, Representative traces for average of 30 EPSP traces before (a) and 26–30 min (b) after HFS_L (This holds for inset traces in all subsequent figures except in *Fig. 3F* and *Fig. 12C*). **D:** LTP magnitudes before and after HFS_L. There was no significant difference between RS and BS (RS/BS, n = 12/13). **E:** *Left,* Representative traces for EPSP summation in control (black) and after application of APV (brown, 50 μM). Right, Mean values for EPSP area in RS [3.0 ± 0.3 mV · s (Con) *vs.* 1.3 ± 0.2 mV · s (APV), n = 5, *p<0.05] and in BS [2.9 ± 0.3 mV · s (Con) *vs.* 1.9 ± 0.1 mV · s (APV), n = 5, *p<0.05]. Note that the APV effect on subthreshold EPSP summation was examined at synapses which have already underwent LTP_{sub}. **F:** Time course of normalized EPSP before and after HFS_L in the presence of APV in both GCs. EPSP amplitude was not potentiated (RS, 1.7 ± 6.0 %, n = 3, light brown; BS, −2.5 ± 4.5 %, n = 4, brown). *Inset*, EPSPs averaged over 1 to 5 min before (a) and after (b) HFS_L. Error bars indicate S.E.M. *p<0.05. n.s., not significant (p>0.05).

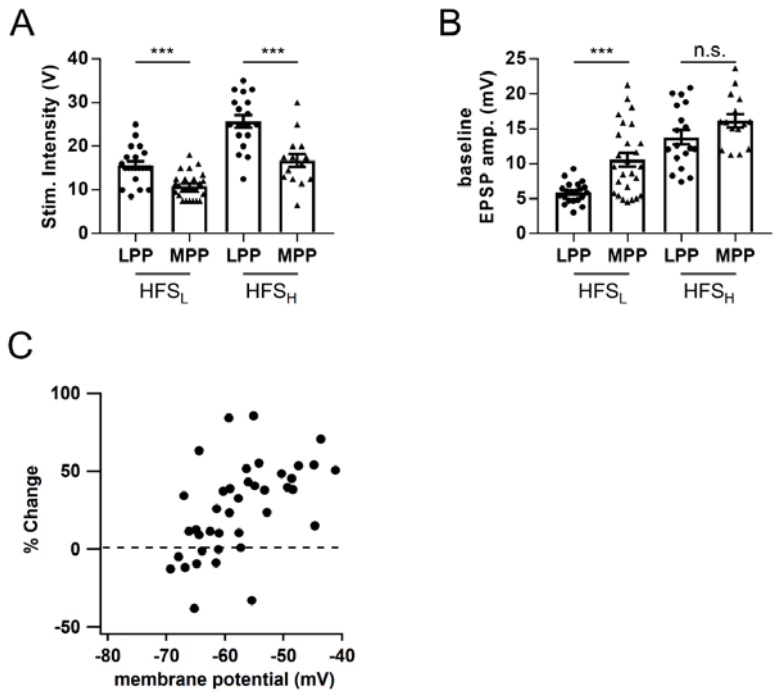

Fig.4, Stimulation Intensities and baseline EPSP amplitudes to evoke sub- or suprathreshold voltage responses at MPP and LPP synapses. A: Mean stimulation intensities used for HFS_L and HFS_H at MPP and LPP synapses. Both mean intensities for HFS_L (LPP, 15.6 ± 0.9 V, n = 21; MPP, 10.9 ± 0.6 V, n = 26; ***p<0.001) and HFS_H (LPP, 25.7 ± 1.4 V, n = 18; MPP, 16.7 ± 1.5 V, n = 15; ***p<0.001) were significantly stronger at LPP-GCs than MPP-GCs. **B:** Baseline amplitudes of EPSP evoked by HFS_L and HFS_H at MPP and LPP synapses. Significantly larger baseline EPSP amplitudes were required at MPP-GCs than LPP-GCs in order to elicit subthreshold responses (HFS_L: LPP, 5.9 ± 0.3 mV, n = 21; MPP,

10.6 ± 1.0 mV, n = 26; ***p<0.001). But, it was not significant to elicit 3 APs responses (HFS_H: LPP, 13.8 ± 1.0 mV, n = 18; MPP, 16.2 ± 1.0 mV, n = 15; p = 0.18). **C:** Plot of LTP_{sub} magnitude as a function of peak membrane potential of EPSP summation. Error bars indicate S.E.M. ***p<0.001. n.s., not significant (p>0.05).

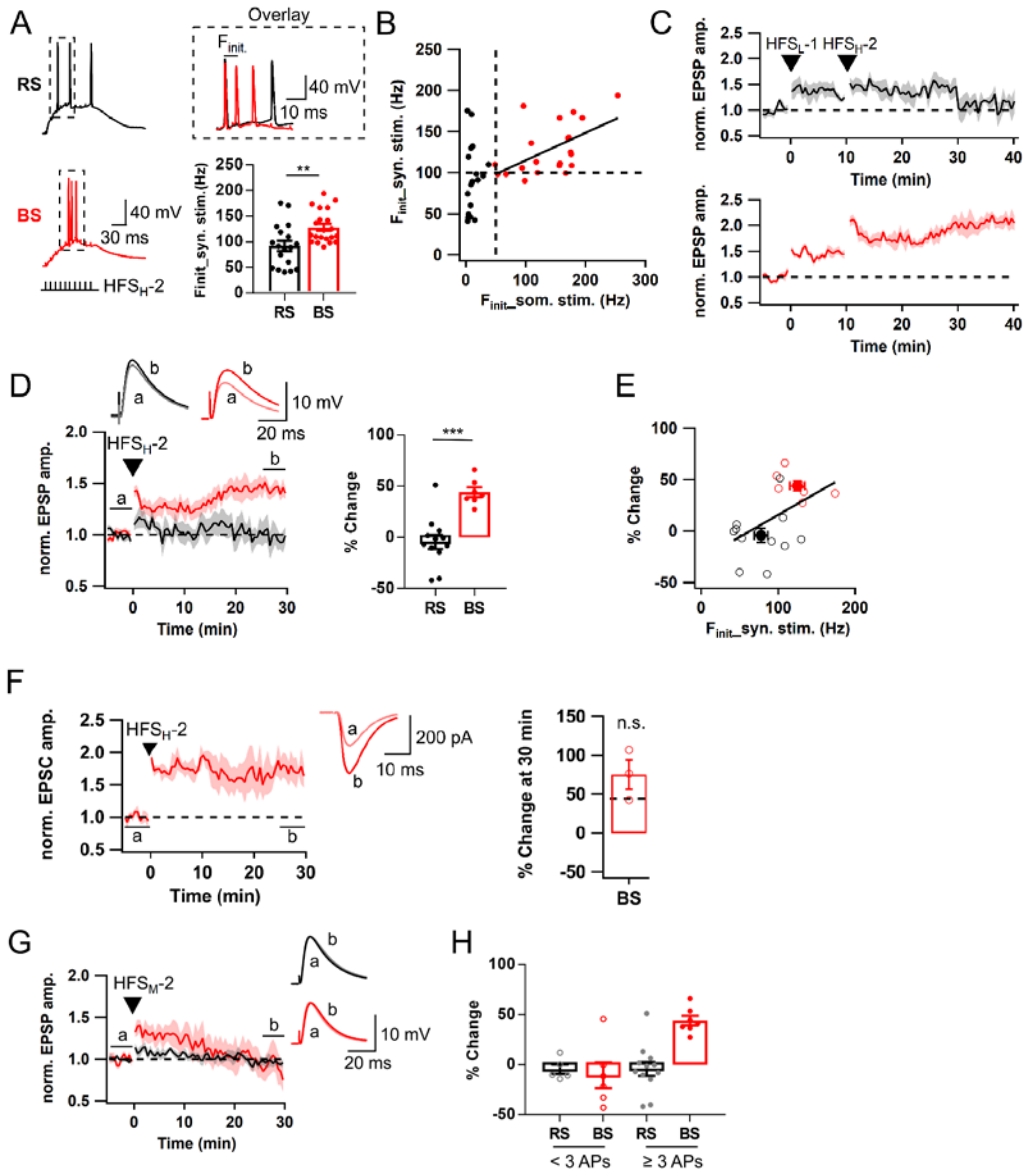

Fig. 5, Hebbian LTP depends on post−synaptic AP bursts, and can be induced only in BS. A: *Left*, Representative voltage responses in RS (gray) and BS (red) to HFS_H−2 which elicited 3 APs. *Right & Upper*, The boxed traces are superimposed for comparison at expanded time scale. *Right & Lower*, Initial AP frequency (F_{init}) of each group (RS/BS, n = 18/21;

p<0.01). **B. Relationship between F_{init} of APs evoked by somatic current injection and that by synaptic stimulation. Two parameters were significantly correlated in BS (r = 0.55, **p<0.01) but not in RS (r = 0.11). Black bold line, linear regression in BS. r, Pearson's correlation coefficient. **C**: Time course of normalized EPSP changes induced by applying two sequential HFS (HFS_L and HFS_H) in RS (black, n = 5) and BS (red, n = 5). Note that LTP_{AP} was induced on top of LTP_{sub} in BS, not in RS. **D**: *Left*, Time course before and after $HFS_{H-}2$. *Right*, Magnitude of LTP_{AP} in RS− and BS−GCs (RS: −4.2 ± 7.0%, n = 12; BS, 44.0 ± 4.8%, n = 7, ***p<0.001). **E**: LTP magnitude as a function of synaptically evoked F_{init}. F_{init} was correlated to LTP magnitude (r = 0.50, *p<0.05). Open circles, individual data; Closed circles, averaged value for each group. Black line, linear regression line. **F**: Similar as in *D*, but the EPSC amplitudes were measured before and after $HFS_{H-}2$ in BS. *Right,* Summary bar graph shows that EPSC potentiation is comparable to averaged value of EPSP potentiation (black dashed line). **G**: Time course of normalized EPSP before and after HFS_M-2. HFS_M-2 is defined by HFS eliciting 1 or 2 APs. Note that LTP was not maintained not only in RS (black) but also in BS (red). **H**: Magnitudes of LTP_{AP} induced by HFS_M or HFS_H in RS and GS (RS, −4.5 ± 4.8%, n = 5; BS, −10.6 ± 12.8 %, n =

6). Error bars indicate S.E.M. **p<0.01. ***p<0.001. n.s., not significant (p>0.05).

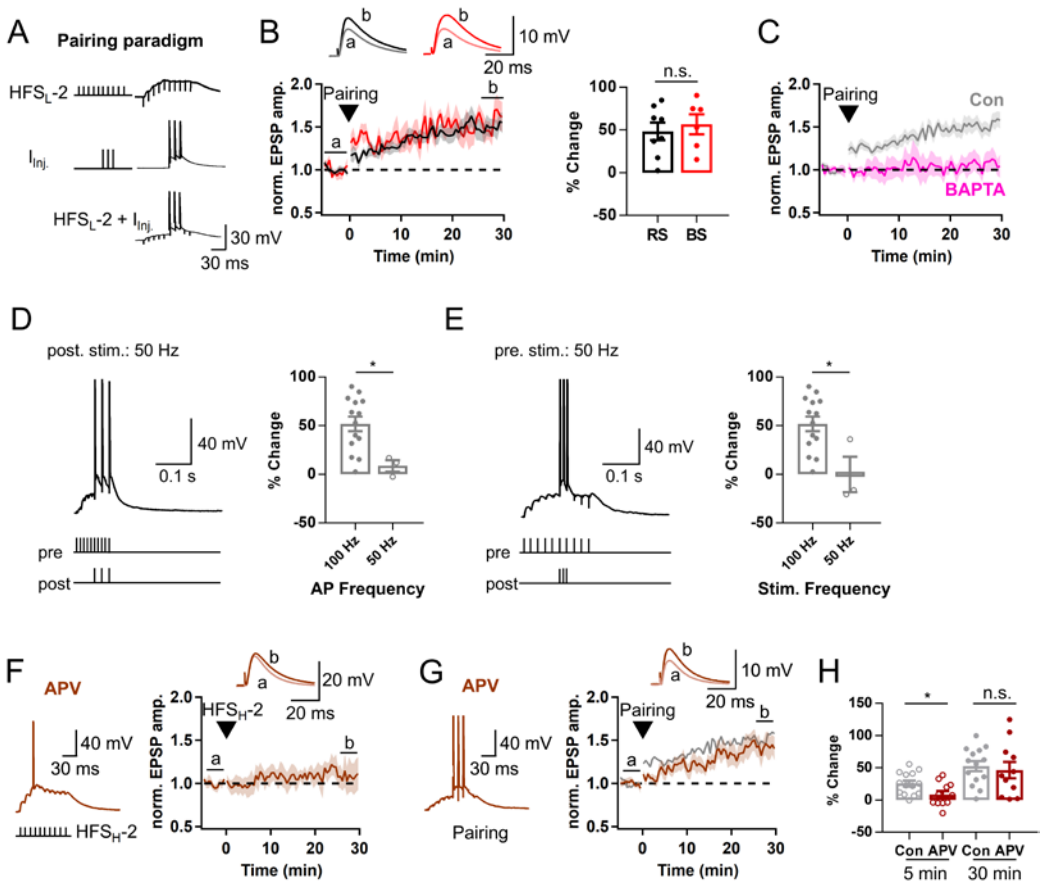

Fig. 6, Conditions for LTP$_{AP}$ induction. **A**: Pairing protocol for LTP$_{AP}$ induction. It consists of subthreshold HFS (HFS$_L$−2) and post−synaptic 3 APs evoked by somatic pulses (2 ms, 3 nA at 100 Hz). **B**: *Left*, Time course of normalized EPSP before and after a pairing protocol. *Right*, Pairing protocol−induced LTP$_{AP}$ in RS− and BS−GCs (RS/BS, n = 8/6). **C**: LTP was not induced in the presence of intracellular solution containing BAPTA (10 mM, pink, n = 7). The control pairing protocol−induced LTP time course is superimposed in gray (n = 14). **D**: Dependence of LTP$_{AP}$

on the postsynaptic AP frequency. When the postsynaptic AP bursts were elicited at 50 Hz instead of 100 Hz in the pairing protocol (*left*), LTP_{AP} was not induced (*right,* 8.7 ± 5.8%, n = 3, *p<0.05). **E:** Dependence of LTP_{AP} on the synaptic stimulation frequency. When ten EPSPs were evoked at 50 Hz instead of 100 Hz in the pairing protocol (*left*), LTP_{AP} was not induced (−0.2 ± 18.2%, n = 3, *p<0.05). **F:** *Left*, Representative voltage traces evoked by HFS_H−2 in the presence of APV (brown, 50 μM). No AP burst was elicited in the presence of APV. *Right*, Time course of normalized EPSP before and after HFS_H−2. **G:** Similar as in *I*, but a pairing protocol was applied instead of HFS_H−2. The control trace (gray) was reproduced from panel H for comparison. **H:** Early (LTP5, open circle) and late phase (LTP30, closed circle) LTP induced by a pairing protocol with and without APV (Control, n = 14; APV, n = 11). Shades and error bars, S.E.M. *p<0.05. n.s., not significant (p>0.05).

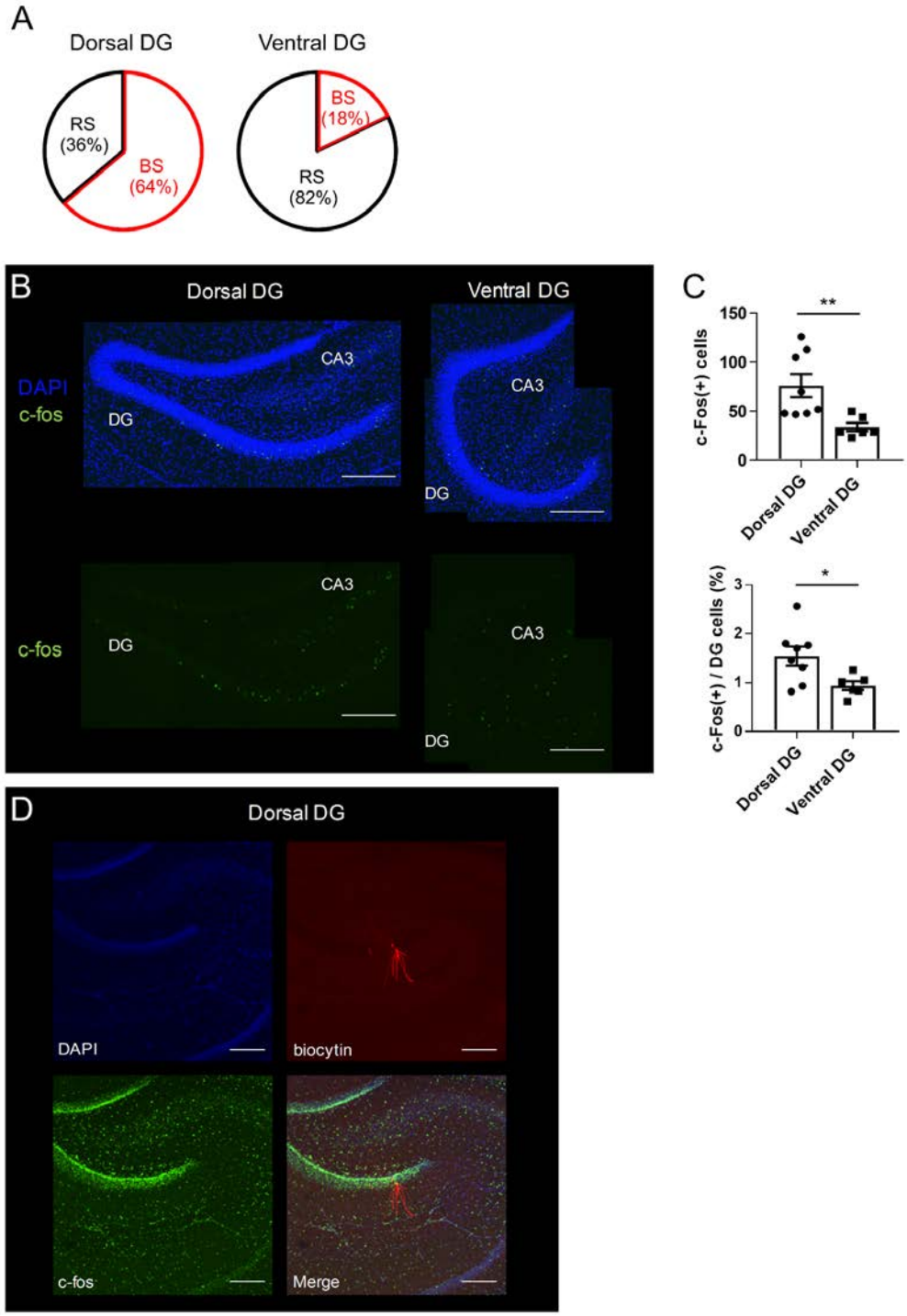
A
Dorsal DG
Ventral DG
RS (36%)
BS (64%)
BS (18%)
RS (82%)
B
Dorsal DG
Ventral DG
DAPI
c-fos
CA3
DG
c-fos
C
c-Fos(+) cells
150
100
50
0
**
Dorsal DG
Ventral DG
c-Fos(+) / DG cells (%)
3
2
1
0
*
D
Dorsal DG
DAPI
biocytin
c-fos
Merge

Fig. 7, Cell distribution and neuronal activity along the dorsoventral axis. **A**: Pie chart showing proportion of RS and BS cells along the dorsoventral axis (RS/BS in dorsal, n = 84/148; in ventral, n = 37/8). **B:** Hippocampal sections from animals exposed novel objects for 1hr. (*Upper*) Merged image show c−fos^{+} cells (green) and DAPI (blue) to visualize GCs in the dorsal (*left*) and ventral (*right*) DG. *Lower*, Images showing c−fos^{+} cells in two regions. Scale bar, 200 μm. **C:** The number of c−fos^{+} cells (*upper*) and the ratio of the number c−fos^{+} cells of the number of GC cells (*lower*) is significantly higher in dorsal DG. **D:** Hippocampal sections to image c−fos signals and cell identification. *Upper & Left*, DAPI was used to visualized GCs. *Upper & Right*, A biocytin filled GC (red). *Lower*, c−fos signals were captured in almost GCs, so it was difficult to distinguish which cells were c−fos^{+}. It might be unreliable results compared to shown in *B*. Scale bar, 200 μm. Error bars indicates S.E.M. *p<0.05, **p<0.01.

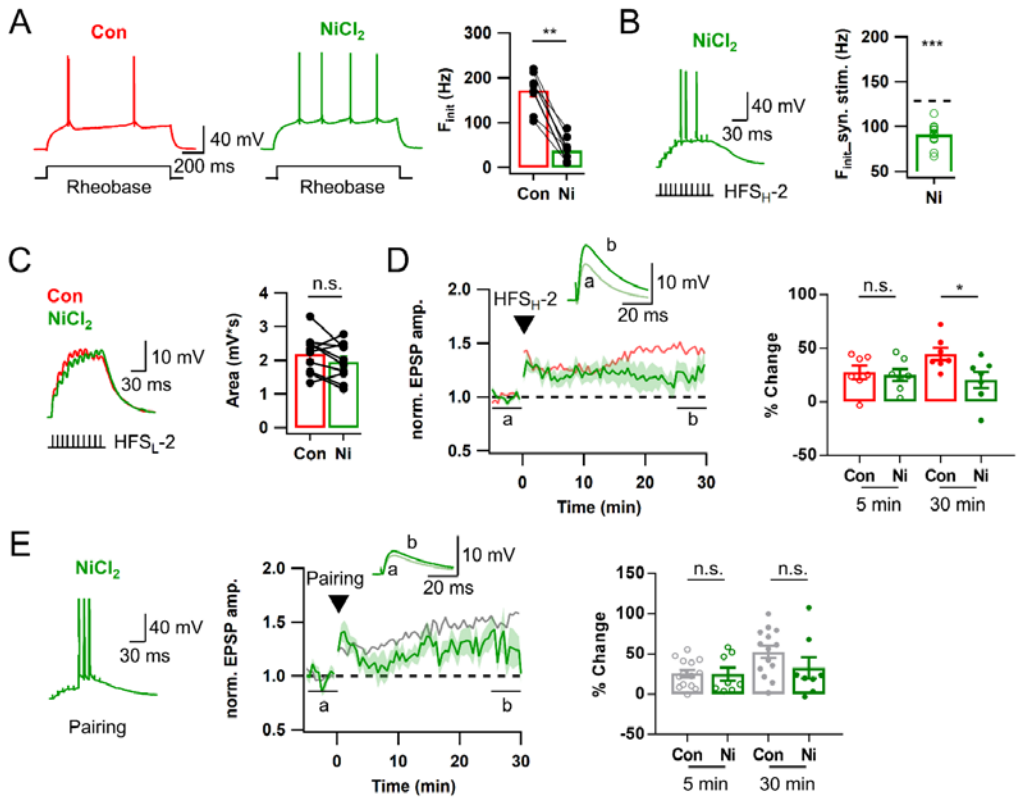

Fig. 8, T-type Ca^{2+} channels contributes to the late phase Hebbian LTP by facilitating AP bursts. A: *Left & Middle*, Voltage responses of a BS cell to somatic rheobase current injection before (red, Con) and after bath application of $NiCl_2$ (50 μM, green). *Right*, Mean values for F_{init} before and after $NiCl_2$ application (n = 9). B: APs evoked by HFS_H-2 in a BS cell (*left*) and their F_{init} (*right*) in the presence of $NiCl_2$ (n = 13). Black dashed line on the bar graph, control mean F_{init} in BS cells (128.3 Hz). C: EPSP summation evoked by HFS_L-2 (*left*) and their area (*right*) before and after applying $NiCl_2$ (Con, 2.2 $\pm$ 0.2 mV · s; $NiCl_2$, 2.0 $\pm$ 0.2 mV · s; n =

10). **D**: *Left*, Time courses of normalized EPSP in BS cells before and after HFS_H−2 with (green) and without (light red) $NiCl_2$. The control time course was reproduced from *Fig. 5D* for comparison. *Right*, Magnitude of HFS_H−induced LTP in the early (LTP5, open circle) and late (LTP30, closed circle) phases in BS cells (Control, n = 7; $NiCl_2$, n = 7). **E**: Similar as in *D*, but evoked by a pairing protocol (Control, n = 14, gray; $NiCl_2$, n = 8, green). Error bars indicate S.E.M. *p<0.05. **p<0.01. ***p<0.001. n.s., not significant (p>0.05).

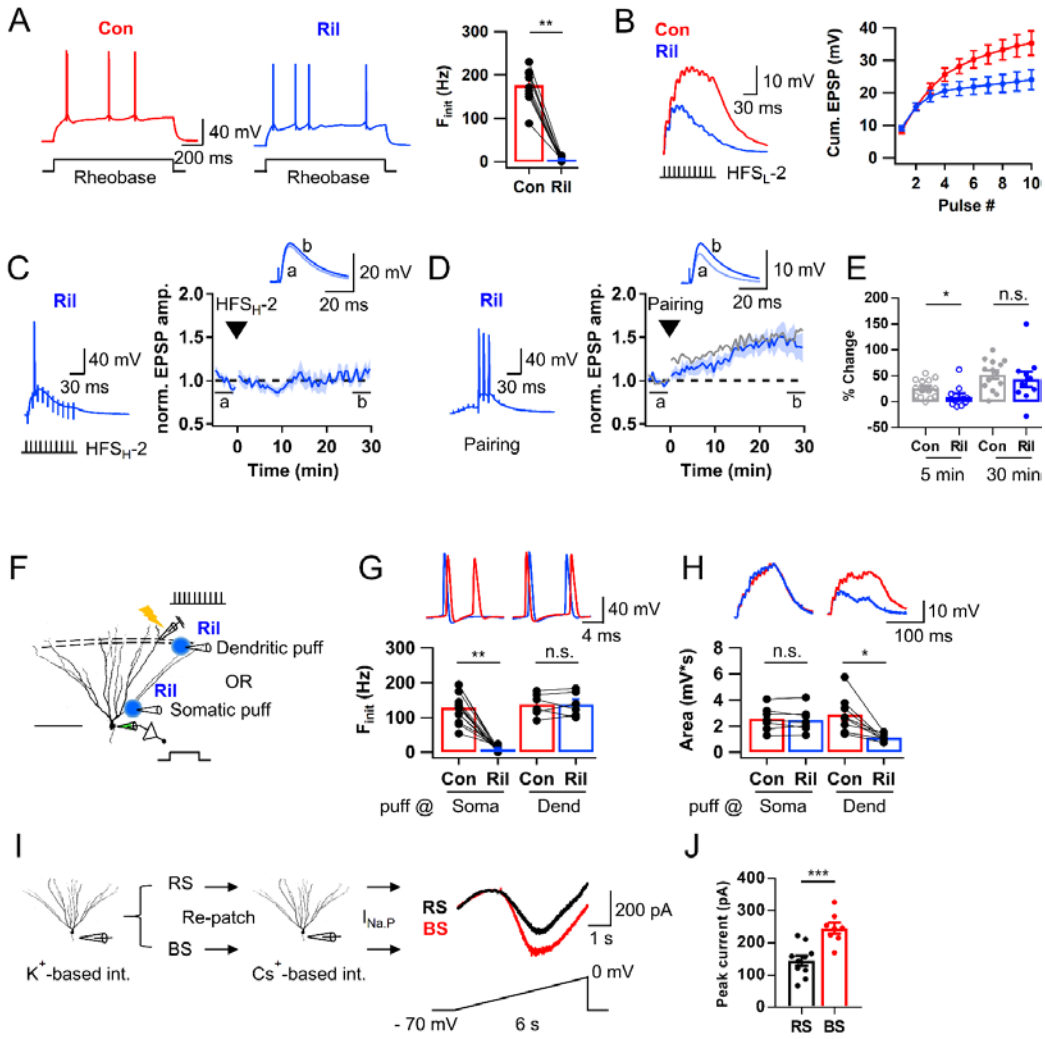

Fig. 9, Persistent Na^+ current ($I_{Na.P}$) amplifies LPP-evoked EPSP summation and is essential for burst firing. A: *Left & Middle*, AP trains in BS elicited by somatic rheobase current injection in control (red, Con) and after applying riluzole (blue, Ril, 10 μM). *Right*, Mean F_{init} before and after application of riluzole (Con, 176.5 ± 12.9 Hz; Ril, 5.7 ± 1.4 Hz; n = 10; **p<0.01). B: *Left*, EPSP summation evoked by HFS_L-2 before and after

applying riluzole. *Right*, Cumulative EPSP amplitudes in control and riluzole conditions (n = 24). **C:** Representative voltage response to HFS_H−2 (*left*) and time course of normalized EPSP before and after HFS_H−2 (*right*, n = 5) in the presence of riluzole. **D:** Similar as in *C*, but evoked by a pairing protocol. **E:** Early (LTP5, open circle) and late phase (LTP30, closed circle) LTP evoked by a pairing protocol in control and riluzole conditions, showing that late LTP_{AP} was rescued (Con, n = 14; Ril, n = 10). **F:** Cartoon for focal application of riluzole (50 μM) at soma or dendrite during somatic current injection or HFS_L of LPP. Scale bar is 100 μm. **G:** Representative traces (*upper*) and mean F_{init} (*lower*) of intrinsic AP bursts with somatic (*left*) and dendritic (*right*) puff of riluzole [Soma, 128.8 ± 12.8 Hz (Con) *vs.* 9.0 ± 3.0 Hz (Ril), n = 12, **p<0.01; Dend, 137.5 ± 13.3 Hz (Con) *vs.* 137.6 ± 14.1 Hz, n = 6]. **H:** Similar as in *G*, but area of subthreshold EPSP summation evoked by HFS_L−2. The EPSP summation was not reduced by somatic puff (*left*) but by dendritic puff (*right*) [Soma, 2.6 ± 0.3 mV · s (Con) *vs.* 2.5 ± 0.4 mV · s (Ril), n = 7; Dend, 2.9 ± 0.5 mV · s (Con) *vs.* 1.1 ± 0.1 mV · s, n = 8]. **I:** *Left*, Procedure for measuring $I_{Na.P}$ in GCs. *Right*, Representative current responses of RS− (black) and BS−GC (red) to a voltage ramp. **J:** Peak current amplitudes of RS and BS cells (RS, 144.9 ± 15.6 pA, n = 10; BS,

245.4 ± 16.4 pA, n = 8; ***p<0.001). Error bars indicate S.E.M. *p<0.05. **p<0.01. ***p<0.001. n.s., not significant (p>0.05).

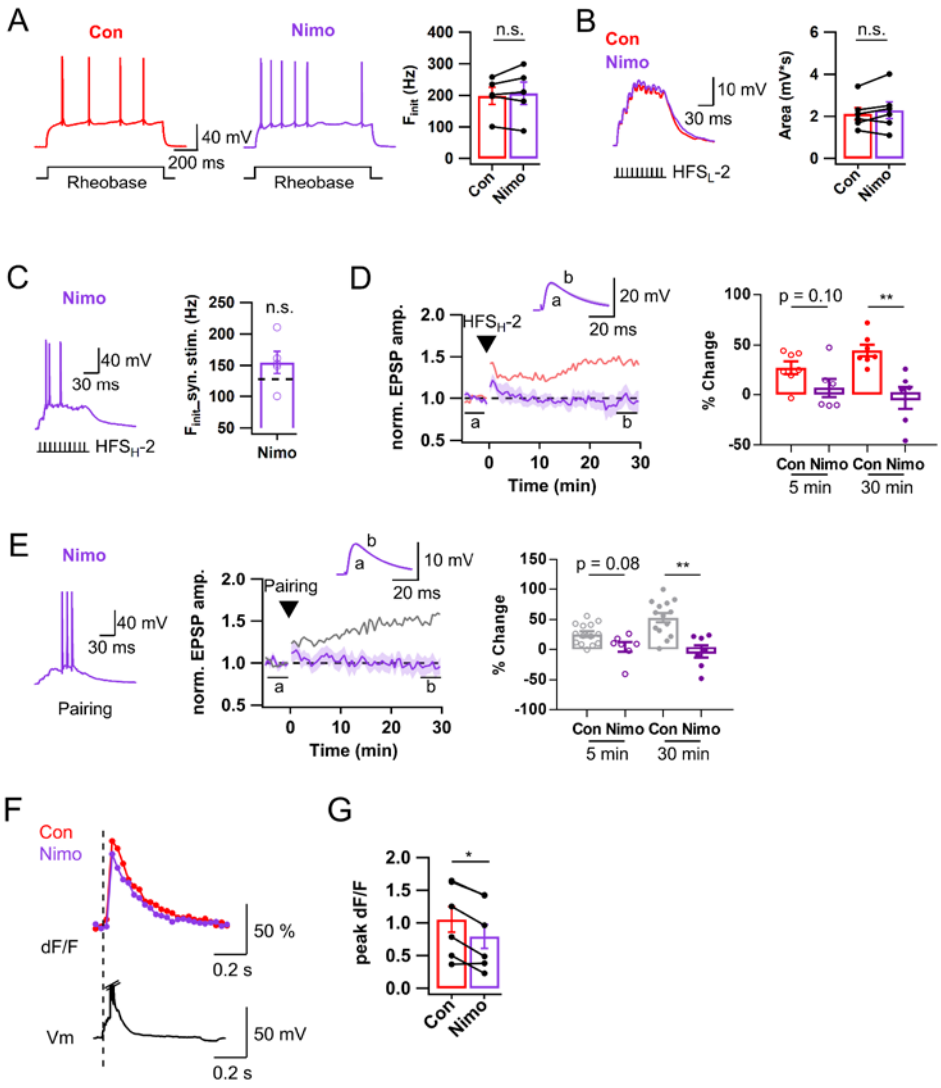

Fig. 10, Ca^{2+} influx through L-type Ca^{2+} channels mediates Hebbian LTP at LPP-GC synapses. A: *Left & Middle*, Representative AP responses to somatic rheobase current injection before (red, Con) and after application of nimodipine (purple, Nimo, 10 μM). *Right*, F_{init} of intrinsic bursts was not affected by nimodipine (Con, 198.3 ± 26.8 Hz; Nimo, 206.7 ± 36.0

Hz; n = 5). **B**: Exemplar traces (*left*) and mean areas (*right*) of EPSP summation evoked by HFS_L−2 of LPP before and after applying nimodipine (Con, 2.1 ± 0.3 mV · s; Nimo, 2.3 ± 0.4 mV · s; n = 6). **C**: Exemplar voltage response of BS−GCs (*left*) evoked by HFS_H−2 and mean F_{init} (*right*) in the presence of nimodipine (Nimo, 154.8 ± 17.5 Hz, n = 5). Black dashed line on the bar graph, control mean F_{init} in BS cells (128.3 Hz). **D**: *Left*, Time course of normalized EPSP in BS−GCs before and after HFS_H−2. *Right*, Magnitudes of early (LTP5, open circle) and late phase (LTP30, closed circle) LTP in control and nimodipine conditions (Con, n = 7; Nimo, n = 6). The control LTP time course and magnitudes were reproduced from *Fig. 5D* (light red). **E**: Similar as in *C*−*D*, but applied a pairing protocol instead of HFS_H. The control LTP trace and magnitudes were reproduced from *Fig. 5H* (gray) (Con, n = 14; Nimo, n = 7). Error bars indicate S.E.M. **p<0.01. n.s., not significant (p>0.05).

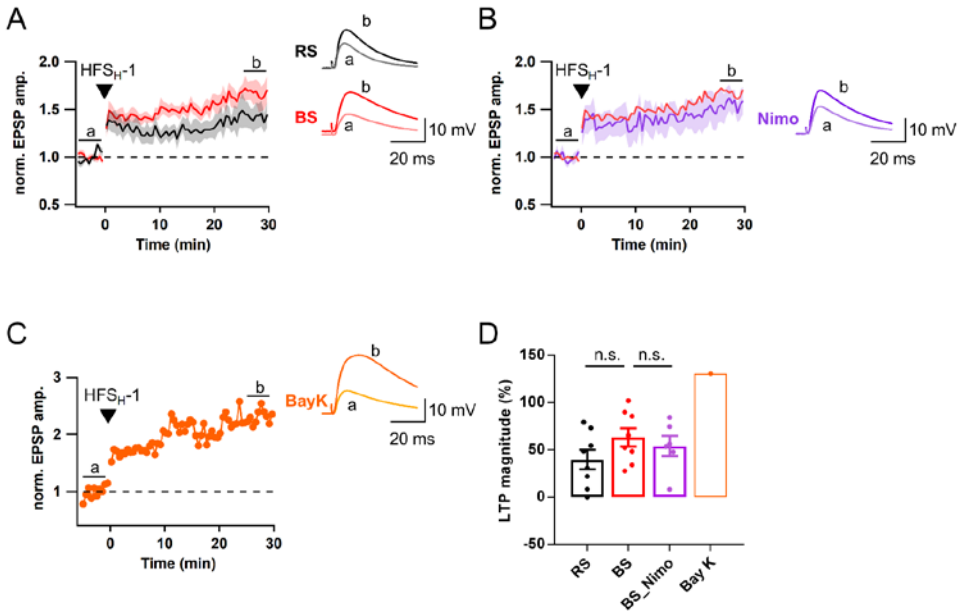

Fig. 11, Further activation of L-VDCC is required for full expression of LTP$_{AP}$. **A:** Time course of normalized EPSP before and after HFS$_H$-1 in RS- (black) and BS-GCs (red). Note that LTP magnitude of BS-GCs did not reach to those induced by sequential stimulation (see Fig. 5C). **B:** Time course of normalized EPSP before and after HFS$_H$-1 in BS-GCs in the presence of nimodipine (purple, Nimo, 10 μM). The control LTP time course was depicted in light red. It indicates that contribution of L-VDCC was relatively smaller than when LTP$_{AP}$ induced HFS$_H$-2.

C: similar as in *B*, but in the presence of Bay K (orange, 10 uM). EPSP amplitude was potentiated by 2-fold. **D:** Summary bar graph showing LTP magnitude in each condition. Error bars indicates S.E.M. n.s., not significant ($p>0.05$).

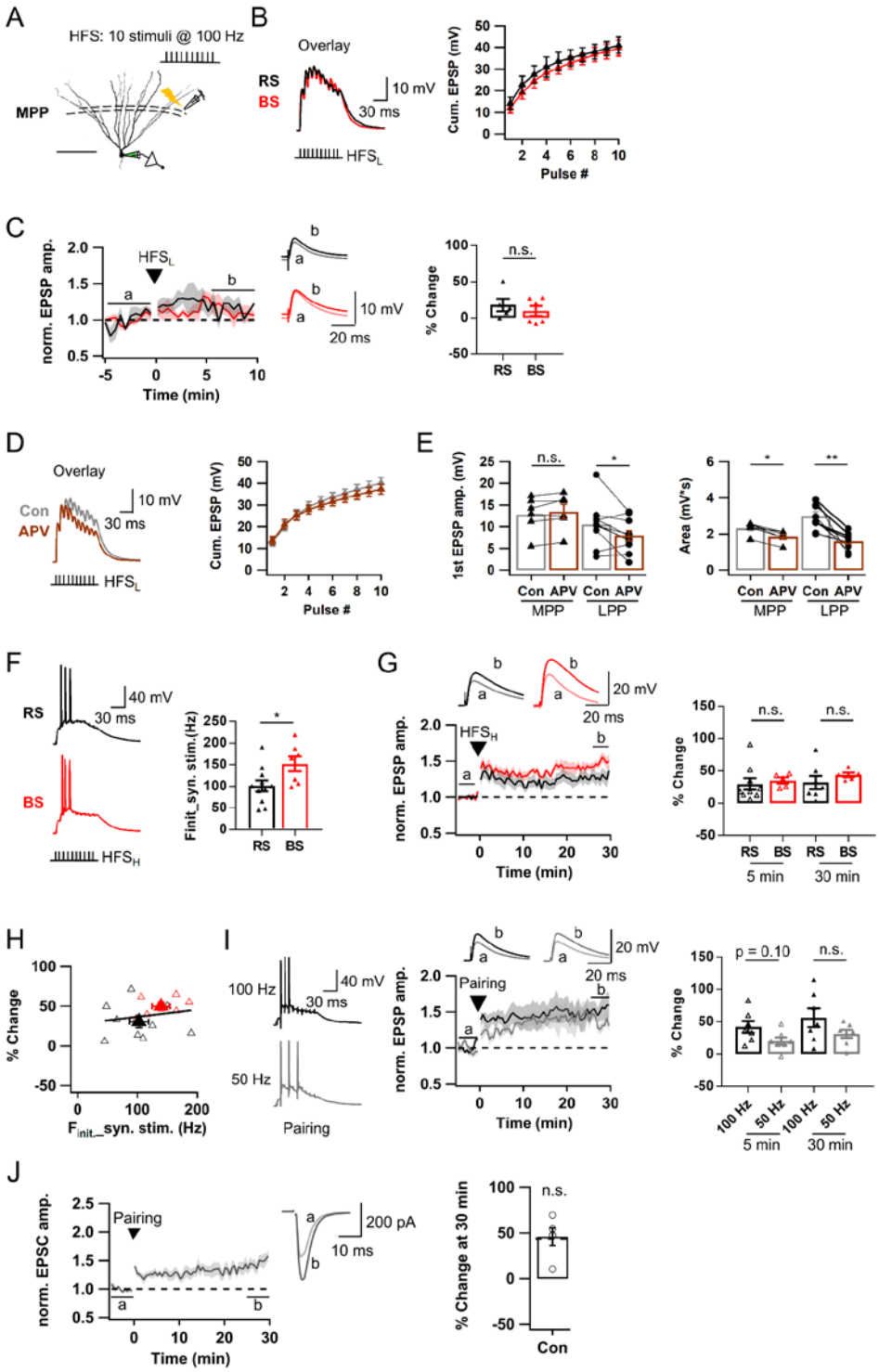
A
HFS: 10 stimuli @ 100 Hz
MPP
B
Overlay
RS
BS
10 mV
30 ms
HFS_L
Cum. EPSP (mV)
Pulse #
C
norm. EPSP amp.
HFS_L
Time (min)
10 mV
20 ms
% Change
n.s.
RS
BS
D
Overlay
Con
APV
10 mV
30 ms
HFS_L
Cum. EPSP (mV)
Pulse #
E
1st EPSP amp. (mV)
n.s.
*
Con APV Con APV
MPP LPP
Area (mV*s)
*
**
Con APV Con APV
MPP LPP
F
RS
BS
40 mV
30 ms
HFS_H
Finit_syn. stim.(Hz)
*
RS
BS
G
20 mV
20 ms
HFS_H
norm. EPSP amp.
Time (min)
% Change
n.s.
n.s.
RS BS RS BS
5 min 30 min
H
% Change
F_init_syn. stim. (Hz)
I
100 Hz
50 Hz
40 mV
30 ms
Pairing
20 mV
20 ms
norm. EPSP amp.
Time (min)
% Change
p = 0.10
n.s.
100 Hz 50 Hz 100 Hz 50 Hz
5 min 30 min
J
norm. EPSC amp.
Pairing
Time (min)
200 pA
10 ms
% Change at 30 min
n.s.
Con

Fig. 12, Postsynaptic AP bursts are not required for LTP induction at MPP−GC synapses. A: Similar as in *Fig.2A*, but medial perforant pathway (MPP) in medial molecular layer was electrically stimulated with a single bout of train pulses (10 stimuli at 100 Hz). Scale bar is 100 μm. **B**: *Left*, Subthreshold voltage responses evoked by HFS_L of MPP in RS− (black) and BS−GCs (red). *Right*, Cumulative EPSP amplitudes of EPSP summation. **C**: *Left*, Time course of normalized EPSP before and after HFS_L of MPP. *Right*, Change in normalized EPSP before and after HFS_L (RS, 17.7 ± 8.8%, n = 5; BS, 9.5 ± 7.0%, n = 6). **D**: *Left*, Representative EPSP summation in control (black) and after application of APV (50 μM, brown). *Right*, Cumulative EPSP amplitudes in control and APV conditions. **E**: *Left*, Mean amplitude of 1^{st} EPSP evoked by a bout of HFS_L in control and APV conditions at MPP and LPP [MPP, 12.8 ± 1.7 mV (Con) *vs.* 13.5 ± 1.7 mV (APV), n = 6; LPP, 9.8 ± 0.9 (Con) *vs.* 7.3 ± 1.1 mV (APV), n = 11, *p < 0.05]. *Right*, Mean area of HFS_L−induced EPSP summation [MPP, 2.3 ± 0.1 mV · s (Con) *vs.* 1.8 ± 0.1 mV · s (APV), n = 6, *p < 0.05; LPP, 3.0 ± 0.2 mV · s (Con) *vs.* 1.6 ± 0.1 mV · s (APV), n = 10, **p<0.01]. Both plots show weaker contribution of NMDAR to EPSPs at MPP−GCs than LPP−GCs. **F**: *Left*, Representative 3 AP bursts evoked by HFS_H in RS− (black) and BS−GCs (red). *Right*,

Initial AP frequency (F_{init}) of each cell type (RS, 101.2 ± 12.7 Hz, n = 11; BS, 152.1 ± 17.3 Hz, n = 7; *p<0.05). **G**: *Left*, Time course of normalized EPSP before and after HFS_H. *Right*, Magnitudes of early (LTP5, open triangle) and late phase (LTP30, closed triangle) LTP, showing that no significant difference in HFS_H-induced LTP_{AP} magnitude between RS- and BS-GCs. **H**: LTP magnitudes as a function of F_{init} of AP bursts evoked by HFS_H at MPP-GCs (r = 0.20, p = 0.47). Open symbols, data of individual cells. Closed symbols, averaged value of each group. Black line, linear regression line. r, Pearson's correlation coefficient. **I**: *Left*, Voltage responses evoked by a pairing protocol comprised of postsynaptic 3 APs at 100 Hz (*upper*, black) or 50 Hz (*lower*, gray) with HFS_L of MPP. *Middle*, Time course of normalized EPSP amplitude before and after the pairing protocol. *Right*, Magnitudes of early (LTP5, open symbols) and late phase (LTP30, closed symbols). Note that no difference was found in LTP_{AP} magnitude between pairing at 100 Hz and even at 50 Hz. **J**: Similar as in *I*, but the EPSC amplitudes were measured before and after pairing protocol in both GCs. *Right,* Summary bar graph shows that EPSC potentiation is comparable to averaged value of EPSP potentiation (black dashed line). Error bars indicate S.E.M. *p<0.05. **p<0.01. n.s., not significant (p>0.05).

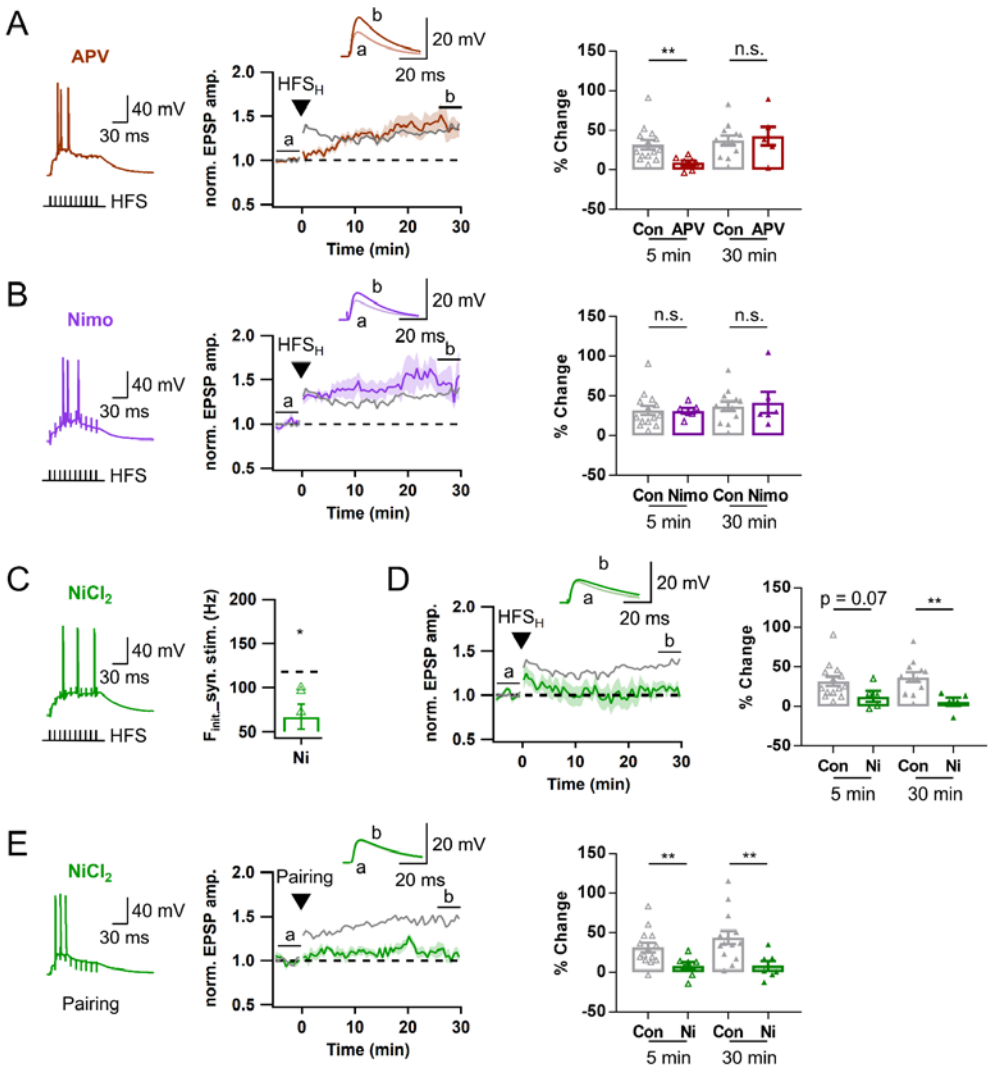

Fig. 13, Ca^{2+} influx through T-type is critical to induce Hebbian LTP at MPP-GCs. For comparison, the LTP time courses and LTP magnitudes of RS and BS in *Fig.7G* are merged and shown as a control LTP time course and magnitude (gray). A: *Left*, Representative voltage response to HFS_H of MPP in the presence of APV (brown, 50 μM). *Middle*, Time course of

normalized EPSP before and after HFS_H. *Right*, Magnitudes of early (LTP5, open triangle) and late phase (LTP30, closed triangle) of LTP, indicating specific reduction of the early phase LTP by APV (Control, n = 12; APV, n = 6). **B:** Similar as in *A*, but in the presence of nimodipine (Nimo, purple, 10 μM). Nimodipine had no significant effect on both early and late LTP_{AP}. (Control: n = 12; Nimo: n = 6). **C:** *Left*, Representative voltage response to HFS_H of MPP in the presence of $NiCl_2$ (green, 50 μM). *Right*, Mean F_{init} in the presence of $NiCl_2$ ($NiCl_2$: 67.0 $\pm$ 14.4 Hz, n = 5). Black dashed line denotes the mean value for F_{init} of both GC types (117.6 Hz, n = 15). **D:** Similar as in *A*, but in the presence of $NiCl_2$ (green). Late phase of LTP was significantly inhibited. **E:** Similar as in *D*, but a pairing protocol was applied of HFS_H. Both early and late LTP is significantly reduced. Error bars indicate S.E.M. *p<0.05. **p<0.01. n.s., not significant (p>0.05).

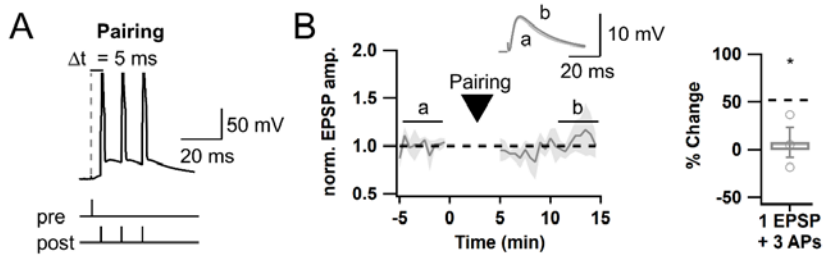

Fig. 14, Single presynaptic stimulation is not sufficient to induce LTP. A: Representative voltage response to a pairing protocol, in which a single EPSP was coupled to 3 APs at 100 Hz (pre−post time interval = 5 ms). **B:** Left, Time course of normalized EPSP before and after applying the pairing protocol shown in *A* 300 times (for 5 min every 1 s). *Right*, LTP_{AP} was not induced by this induction protocol (7.8 ± 15.9%, n = 3, *p<0.05). Black dashed line, mean value for LTP magnitude induced by a conventional pairing protocol comprised of 10 EPSPs and 3 APs as shown in *Figure 15I*.

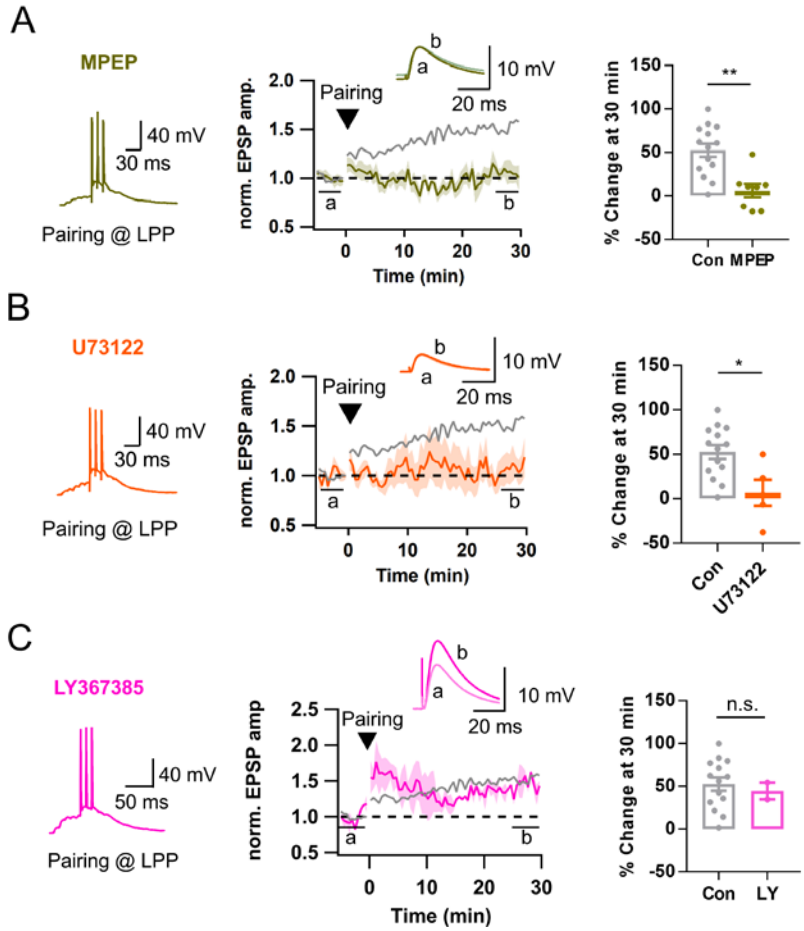

Fig. 15, mGluR5−PLC activation is involved in LTP at LPP−GCs. A: *Left*, Representative voltage response to a pairing protocol at LPP−GC synapse in the presence of MPEP (dark green, 25 μM). *Middle*, Time course of normalized EPSP before and after applying a pairing protocol. *Right*, Magnitudes late phase (LTP30, closed circle) of LTP in the presence of MPEP [6.0 ± 7.7% *vs.* 52.6 ± 7.7%, MPEP (n = 8) *vs.* Con (n = 14), **p<0.01]. B: Similar as in *A*, but in the presence of U73122 (orange, 2

μM). Late LTP_{AP} were significantly inhibited [6.7 ± 14.6% *vs.* 52.6 ± 7.7%, U73122 (n = 5) *vs.* Con (n = 14), *p<0.05]. C: Similar as in *A*, in the presence of LY367385 (pink, 50 μM). Magnitudes in late phase (closed circle) of LTP in the presence of LY367385 [44.5 ± 10.0% *vs.* 52.6 ± 7.7%, LY (n = 2) *vs.* Con (n = 14)]. Note that LTP was intact in blockade of mGluR1. For comparison of LTP at LPP synapses in *A*–*C*, the time courses and magnitudes of LTP induced by a pairing protocol are reproduced from *Fig. 5H* (gray). Error bars indicate S.E.M. *p<0.05. **p<0.01. n.s., not significant (p>0.05).

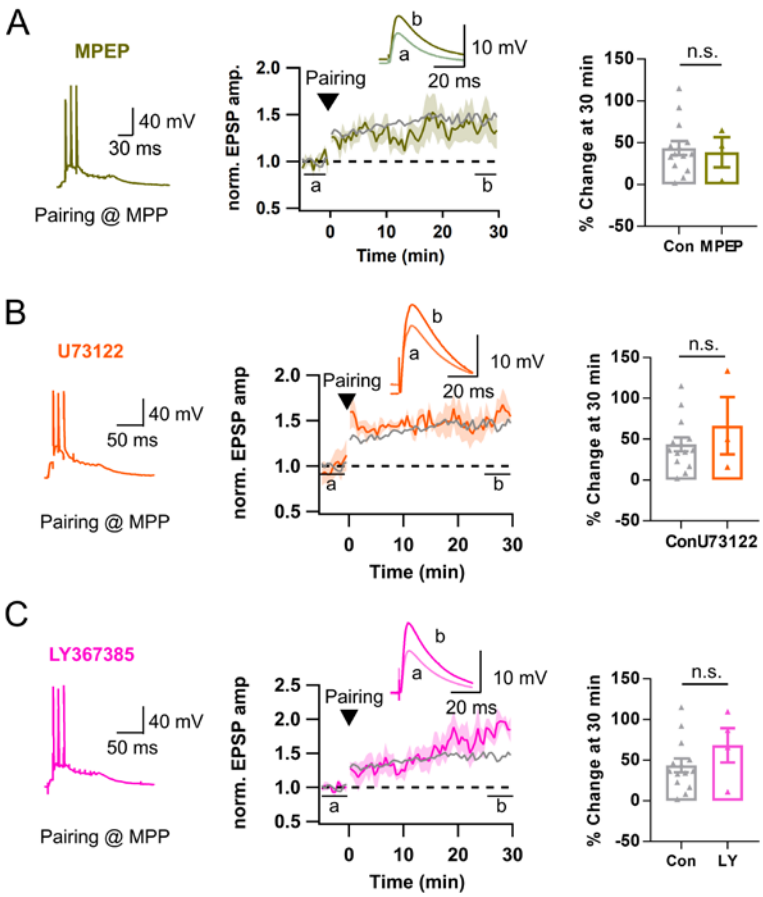

Fig. 16, mGluR1/5−PLC activation is not involved in LTP at MPP−GCs. A: Similar as in *Fig15*, but the pairing protocol applied at MPP−GCs. *Left*, Representative voltage response to a pairing protocol in the presence of MPEP (dark green, 25 μM). *Middle*, Time course of normalized EPSP before and after applying a pairing protocol. *Right*, Magnitudes late phase (LTP30, closed triangle) of LTP in the presence of MPEP [38.7 ± 18.8% *vs.* 43.7 ± 8.4%; MPEP (n = 3) *vs.* Con (n = 14)]. **B:** Similar as in *A*, but in the presence of U73122 (orange, 2 μM). Late phase of LTP_{AP} were

not affected by U73122 [66.5 ± 35.0% *vs.* 43.7 ± 8.4%; U73122 (n = 3) *vs.* Con (n = 14)]. C: Similar as in *A*, in the presence of LY367385 (pink, 50 μM). Late LTP_{AP} were not affected by LY367385 [68.4 ± 21.1% *vs.* 43.7 ± 8.4%, LY (n = 4) *vs.* Con (n = 14)]. For comparison of LTP at MPP synapses in *A*–*C*, the time courses and magnitudes of LTP induced by the pairing protocol are reproduced from *Fig. 12I.* Error bars indicate S.E.M. n.s., not significant ($p>0.05$).

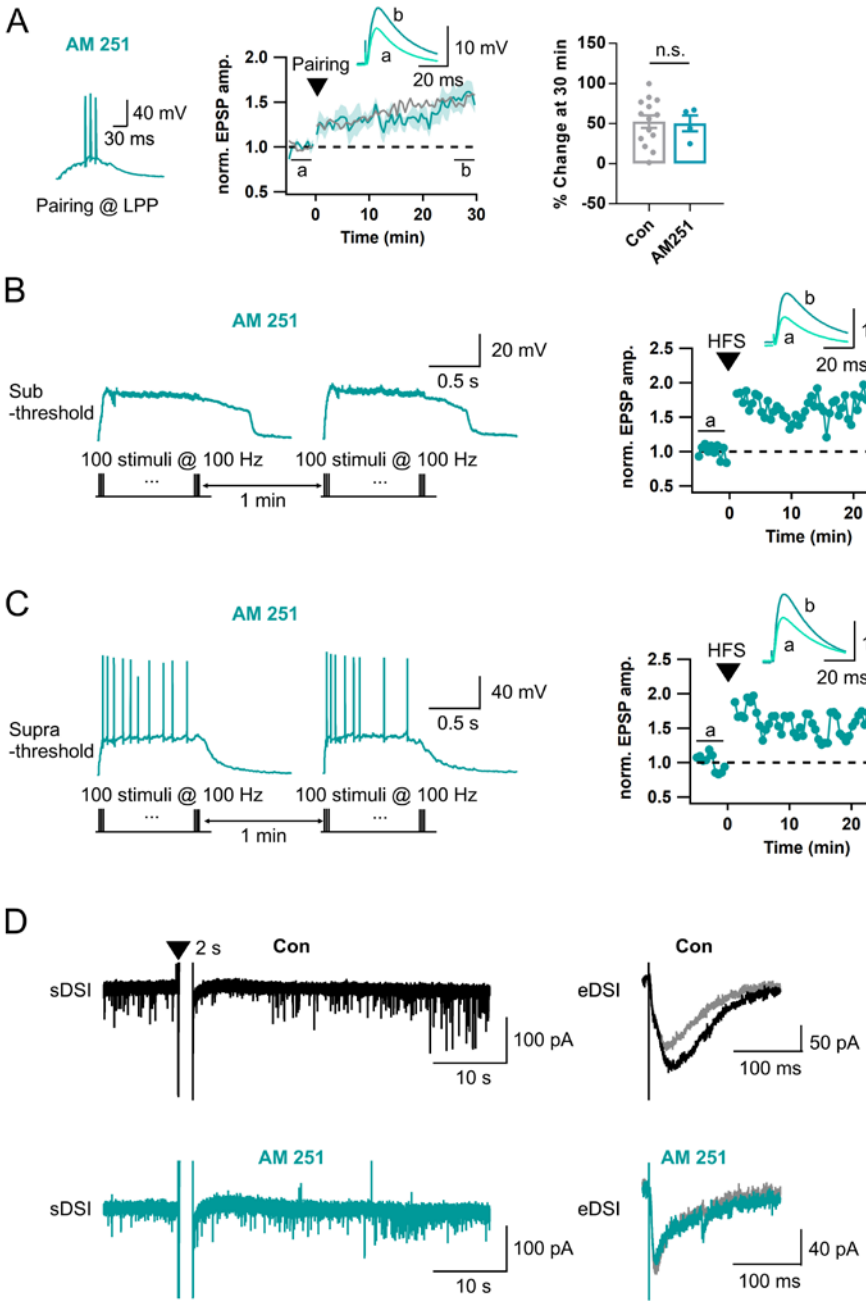
A
AM 251
40 mV
30 ms
Pairing @ LPP
Pairing
20 ms
10 mV
norm. EPSP amp.
Time (min)
% Change at 30 min
n.s.
Con
AM251
B
AM 251
20 mV
0.5 s
Sub
-threshold
100 stimuli @ 100 Hz
100 stimuli @ 100 Hz
1 min
HFS
C
AM 251
40 mV
0.5 s
Supra
-threshold
D
2 s
Con
sDSI
100 pA
10 s
eDSI
50 pA
100 ms
AM 251
40 pA

Fig. 17, Endocannabinoid signaling is not associated with LTP_{sub} and LTP_{AP} at LPP−GCs. A: Similar as in *Fig15*, but in the presence of AM 251 (light blue, 5 μM). Late LTP_{AP} were not affected by AM251 [50.3 ± 9.9% *vs.* 52.6 ± 7.7%; AM 251 (n = 4) *vs.* Con (n = 14)]. **B:** *Left*, Representative subthreshold response to two trains of HFS (100 pulses at 100 Hz, 1 min interval). *Right*, Time course of normalized EPSP before and after two trains of HFS indicates EPSP amplitude is potentiated (70.6%, n = 1). **C:** Similar as in *B*, but suprathreshold level. EPSP amplitude is potentiated as well (57.1 %, n = 1).

D: Experiments to confirm working activity of AM 251. *Upper*, Representative trace shows spontaneous and evoked IPSC. Depolarization−induced suppression of inhibition (DSI) was evoked by depolarizing voltage step (from −70 mV to 0 mV, 2 s duration) and tested in two methods (sDSI: spontaneous DSI, *left*; eDSI: evoked DSI, *right*) in control. *Lower*, Representative trace of both DSI in the presence of AM 251. Note that both DSI were disappeared in the presence of AM 251.

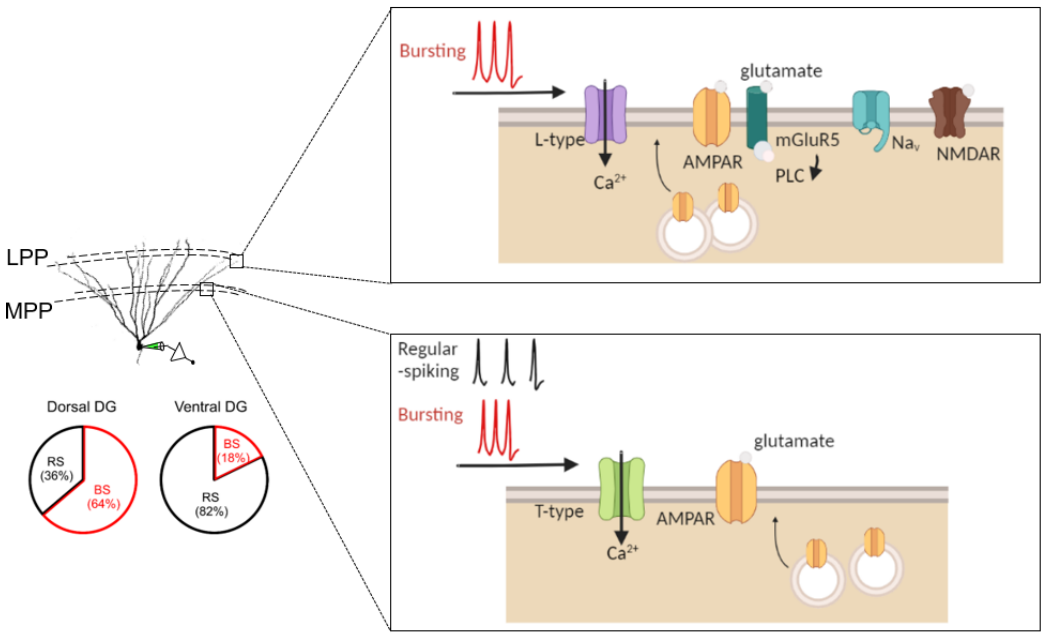

Fig. 18, Understanding modulation of long-term potentiation by firing patterns at LPP- and MPP-GC synapses. The synaptic inputs are considerably boosted by NMDAR and $I_{Na.P}$. Summated EPSPs over threshold membrane potential give rise to generate APs. The majority of GCs fires in burst manner in dorsal DG. High frequency bAPs of BS readily induce LTP by specifically activating L-type Ca^{2+} channels at LPP-GCs in accompany with mGluR5 signaling pathway. However, regardless of cell types, bAPs of both BS and RS cells could induce LTP at MPP-GCs by activating T-type Ca^{2+} channels.

REFERENCES

Alme C, Buzzetti R, Marrone D, Leutgeb J, Chawla M, Schaner M, Bohanick J, Khoboko T, Leutgeb S, Moser E (2010) Hippocampal granule cells opt for early retirement. Hippocampus 20:1109–1123.

Bayazitov IT, Richardson RJ, Fricke RG, Zakharenko SS (2007) Slow presynaptic and fast postsynaptic components of compound long–term potentiation. Journal of Neuroscience 27:11510–11521.

Bittner KC, Milstein AD, Grienberger C, Romani S, Magee JC (2017) Behavioral time scale synaptic plasticity underlies CA1 place fields. Science 357:1033–1036.

Bliss TV, Lømo T (1973) Long-lasting potentiation of synaptic transmission in the dentate area of the anaesthetized rabbit following stimulation of the perforant path. The Journal of physiology 232:331–356.

Chen C, Satterfield R, Young Jr SM, Jonas P (2017) Triple function of synaptotagmin 7 ensures efficiency of high–frequency transmission at central GABAergic synapses. Cell reports 21:2082–2089.

Chen S, Yue C, Yaari Y (2005) A transitional period of Ca2+-dependent spike afterdepolarization and bursting in developing rat CA1

pyramidal cells. The Journal of physiology 567:79–93.

Claiborne BJ, Amaral DG, Cowan WM (1990) Quantitative, three-dimensional analysis of granule cell dendrites in the rat dentate gyrus. Journal of Comparative Neurology 302:206–219.

Colino A, Malenka RC (1993) Mechanisms underlying induction of long-term potentiation in rat medial and lateral perforant paths in vitro. Journal of neurophysiology 69:1150–1159.

Diamantaki M, Frey M, Berens P, Preston-Ferrer P, Burgalossi A (2016) Sparse activity of identified dentate granule cells during spatial exploration. Elife 5:e20252.

Dong H-W, Swanson LW, Chen L, Fanselow MS, Toga AW (2009) Genomic–anatomic evidence for distinct functional domains in hippocampal field CA1. Proceedings of the National Academy of Sciences 106:11794–11799.

Dumenieu M, Senkov O, Mironov A, Bourinet E, Kreutz MR, Dityatev A, Heine M, Bikbaev A, Lopez-Rojas J (2018) The low-threshold calcium channel Cav3. 2 mediates burst firing of mature dentate granule cells. Cerebral Cortex 28:2594–2609.

Fanselow MS, Dong H-W (2010) Are the dorsal and ventral hippocampus functionally distinct structures? Neuron 65:7–19.

Grover LM, Teyler TJ (1990) Two components of long-term potentiation induced by different patterns of afferent activation. Nature 347:477-479.

Hönigsperger C, Marosi M, Murphy R, Storm JF (2015) Dorsoventral differences in Kv7/M-current and its impact on resonance, temporal summation and excitability in rat hippocampal pyramidal cells. The Journal of physiology 593:1551-1580.

Hsu C-L, Zhao X, Milstein AD, Spruston N (2018) Persistent sodium current mediates the steep voltage dependence of spatial coding in hippocampal pyramidal neurons. Neuron 99:147-162. e148.

Hsu T-T, Lee C-T, Tai M-H, Lien C-C (2016) Differential recruitment of dentate gyrus interneuron types by commissural versus perforant pathways. Cerebral cortex 26:2715-2727.

Hunt DL, Linaro D, Si B, Romani S, Spruston N (2018) A novel pyramidal cell type promotes sharp-wave synchronization in the hippocampus. Nature neuroscience 21:985-995.

Jackman SL, Turecek J, Belinsky JE, Regehr WG (2016) The calcium sensor synaptotagmin 7 is required for synaptic facilitation. Nature 529:88-91.

Kampa BM, Letzkus JJ, Stuart GJ (2006) Requirement of dendritic calcium

spikes for induction of spike-timing-dependent synaptic plasticity. The Journal of physiology 574:283–290.

Kim S, Jung D, Royer S (2020) Place cell maps slowly develop via competitive learning and conjunctive coding in the dentate gyrus. Nature communications 11:1–15.

Kim S, Kim Y, Lee S–H, Ho W–K (2018) Dendritic spikes in hippocampal granule cells are necessary for long–term potentiation at the perforant path synapse. Elife 7:e35269.

Krueppel R, Remy S, Beck H (2011) Dendritic integration in hippocampal dentate granule cells. Neuron 71:512–528.

Larkum ME, Kaiser K, Sakmann B (1999) Calcium electrogenesis in distal apical dendrites of layer 5 pyramidal cells at a critical frequency of back–propagating action potentials. Proceedings of the National Academy of Sciences 96:14600–14604.

Letzkus JJ, Kampa BM, Stuart GJ (2006) Learning rules for spike timing–dependent plasticity depend on dendritic synapse location. Journal of Neuroscience 26:10420–10429.

Lisman J (2017) Glutamatergic synapses are structurally and biochemically complex because of multiple plasticity processes: long–term potentiation, long–term depression, short–term

potentiation and scaling. Philosophical Transactions of the Royal Society B: Biological Sciences 372:20160260.

Lisman JE (1997) Bursts as a unit of neural information: making unreliable synapses reliable. Trends in neurosciences 20:38–43.

Llinás RR, Steriade M (2006) Bursting of thalamic neurons and states of vigilance. Journal of neurophysiology 95:3297–3308.

Lopez–Rojas J, Kreutz MR (2016) Mature granule cells of the dentate gyrus—Passive bystanders or principal performers in hippocampal function? Neuroscience & Biobehavioral Reviews 64:167–174.

Marcelin B, Lugo JN, Brewster AL, Liu Z, Lewis AS, McClelland S, Chetkovich DM, Baram TZ, Anderson AE, Becker A (2012) Differential dorso–ventral distributions of Kv4. 2 and HCN proteins confer distinct integrative properties to hippocampal CA1 pyramidal cell distal dendrites. Journal of Biological Chemistry 287:17656–17661.

Okubo Y, Iino M (2011) Visualization of glutamate as a volume transmitter. The Journal of Physiology 589:481–488.

Pernía–Andrade AJ, Jonas P (2014) Theta–gamma–modulated synaptic currents in hippocampal granule cells in vivo define a mechanism for network oscillations. Neuron 81:140–152.

Petrovich GD, Canteras NS, Swanson LW (2001) Combinatorial amygdalar inputs to hippocampal domains and hypothalamic behavior systems. Brain research reviews 38:247-289.

Pignatelli M, Ryan TJ, Roy DS, Lovett C, Smith LM, Muralidhar S, Tonegawa S (2019) Engram cell excitability state determines the efficacy of memory retrieval. Neuron 101:274-284. e275.

Raus Balind S, Magó Á, Ahmadi M, Kis N, Varga-Németh Z, Lőrincz A, Makara JK (2019) Diverse synaptic and dendritic mechanisms of complex spike burst generation in hippocampal CA3 pyramidal cells. Nature communications 10:1-15.

Remy S, Spruston N (2007) Dendritic spikes induce single-burst long-term potentiation. Proceedings of the National Academy of Sciences 104:17192-17197.

Ryan TJ, Roy DS, Pignatelli M, Arons A, Tonegawa S (2015) Engram cells retain memory under retrograde amnesia. Science 348:1007-1013.

Schmidt-Hieber C, Jonas P, Bischofberger J (2004) Enhanced synaptic plasticity in newly generated granule cells of the adult hippocampus. Nature 429:184-187.

Schreurs A, Sabanov V, Balschun D (2017) Distinct properties of long-term potentiation in the dentate gyrus along the dorsoventral axis:

influence of age and inhibition. Scientific reports 7:1-10.

Schwindt PC, Crill WE (1995) Amplification of synaptic current by persistent sodium conductance in apical dendrite of neocortical neurons. Journal of neurophysiology 74:2220-2224.

Strange BA, Witter MP, Lein ES, Moser EI (2014) Functional organization of the hippocampal longitudinal axis. Nature Reviews Neuroscience 15:655-669.

Wang W, Trieu BH, Palmer LC, Jia Y, Pham DT, Jung K-M, Karsten CA, Merrill CB, Mackie K, Gall CM (2016) A primary cortical input to hippocampus expresses a pathway-specific and endocannabinoid-dependent form of long-term potentiation. Eneuro 3.

Watanabe S, Hoffman DA, Migliore M, Johnston D (2002) Dendritic K+ channels contribute to spike-timing dependent long-term potentiation in hippocampal pyramidal neurons. Proceedings of the National Academy of Sciences 99:8366-8371.

Wu J, Harney S, Rowan MJ, Anwyl R (2008) Involvement of group I mGluRs in LTP induced by strong high frequency stimulation in the dentate gyrus in vitro. Neuroscience letters 436:235-238.

Yasuda R, Sabatini BL, Svoboda K (2003) Plasticity of calcium channels in dendritic spines. Nat Neurosci 6:948-955.

Yue C, Remy S, Su H, Beck H, Yaari Y (2005) Proximal persistent Na+ channels drive spike afterdepolarizations and associated bursting in adult CA1 pyramidal cells. Journal of Neuroscience 25:9704–9720.

Zhang X, Schlögl A, Jonas P (2020) Selective routing of spatial information flow from input to output in hippocampal granule cells. Neuron 107:1212–1225. e1217.

초 록

뉴런의 폭발적 발화는 활동전위(AP)가 역전파 될 때, 수상돌기 막 전위를 효과적으로 탈분극 시켜 시냅스 가소성을 유도 할 수 있다. 해마 치상회절(DG)의 과립세포(GC)에서 나타나는 폭발적 발화의 생리학적 중요성은 아직 알려지지 않았다. 본 연구자는 성숙한 과립세포에 패치클램프 방법을 이용하여 전류 주입 시 초기 발화 빈도에 따라 규칙적 발화(RS) 세포와 폭발적 발화(BS) 세포로 분류하였다. 두 가지 유형의 과립세포가 높은 주파수 외측천공경로(LPP)와 내측천공경로(MPP) 입력에 어떻게 반응하는 지 관찰하였다. 외측천공경로 시냅스에서 Hebbian 장기강화를 유도하려면 100 Hz 보다 높은 초기 주파수(F_{init})를 수반하는 최소 3개의 활동 전위(AP)가 필요함을 확인했다. 이 반응은 폭발적 발화 세포에서만 특이적으로 나타남을 확인하였다.

폭발적 발화는 지속적인 Na^+ 전류에 크게 의존하는데, 이 전류의 크기가 폭발적 발화 세포에서 규칙적 발화세포보다 크게 나타남을 밝혔다. L-형 칼슘 채널이 외측천공경로 시냅스에서의 Hebbian 장기강화에 필요한 Ca^{2+} 을 제공한다. 하지만, 내측천공경로 시냅스에서의 Hebbian 장기강화는 T-형 칼슘 채널에 의해 매개되었고, 세포 유형 또는 시냅스 후 활동전압의 빈도에 관계없이 유도될 수 있었다. 이러한 결과는 고유 발화 특성이 시냅스 입력에 의한 발화에 영향을 미치고 폭발적 발화 패턴이 시냅스 입력 경로에 따라 Hebbian 장기강화 메커니즘에 차등적으로 영향을 미친다는 것을 시사한다.

주요어 : 폭발적 발화세포, 규칙적 발화세포, Hebbian 장기강화, L-형 칼슘 채널, T-형 칼슘 채널, 지속성 나트륨 전류, 천공경로

학 번 : 2016-21976